REVIEW ARTICLE (INVITED ONLY)

Advances in Flexible, Foldable, and Stretchable Quantum Dot Light-Emitting Diodes: Materials and Fabrication Strategies

Taewoo Park[1] · Ji Su Kim[2,3] · Daewon Ko[1] · Gi Doo Cha[4] · Dae-Hyeong Kim[2,3] · Dong Chan Kim[1,5]

Abstract

Deformable light-emitting devices, capable of maintaining consistent light emission even under mechanical deformations, represent a cornerstone for next-generation human-centric electronics. Quantum dot light-emitting diodes (QLEDs), leveraging the electroluminescence (EL) of colloidal quantum dots (QDs), show exceptional promise in this domain. Their superior advantages, such as excellent color purity, high luminous efficiency, slim form factor, and facile fabrication on various soft substrates, position them as prime candidates for deformable EL devices. This review explores recent advancements in deformable QLEDs, with a particular focus on material engineering and fabrication strategies. We begin by introducing various types of QDs and the operational principles of QLEDs, along with summarizing performance enhancements in reported deformable devices. Next, we categorize device structures based on the direction of light emission. We then discuss representative methods for patterning QD thin films on flexible substrates to fabricate full-color QLEDs. Additionally, we highlight fabrication strategies for deformable QLEDs with unconventional form factors, including flexible, foldable, fiber-type, and stretchable devices, and their potential applications. We conclude this review with a brief outlook on the future of this technology.

Keywords Quantum dot light-emitting diodes (QLEDs) · Flexible QLEDs · Foldable QLEDs · Stretchable QLEDs

Taewoo Park, Ji Su Kim, and Daewon Ko contributed equally to this work.

✉ Dae-Hyeong Kim
  dkim98@snu.ac.kr

✉ Dong Chan Kim
  dckim@gachon.ac.kr

1 Department of Chemical and Biological Engineering, Gachon University, Seongnam-si, Gyeonggi-do 13120, Republic of Korea

2 Center for Nanoparticle Research, Institute for Basic Science (IBS), Seoul 08826, Republic of Korea

3 School of Chemical and Biological Engineering, Institute of Chemical Processes, Seoul National University, Seoul 08826, Republic of Korea

4 Department of Systems Biotechnology, Chung-Ang University, Anseong 17546, Republic of Korea

5 Department of Semiconductor Engineering, Gachon University, Seongnam-si, Gyeonggi-do 13120, Republic of Korea

Introduction

Emergence of Deformable Light-Emitting Devices

Over the past decades, soft electronics have emerged as promising alternatives to traditional rigid electronics, particularly for next-generation human-friendly electronics applications [1–3]. Their soft and flexible nature, closely mimicking the mechanical properties of the human body, allows for seamless integration without causing discomfort. This deformable nature not only enhances the interaction between the device and the users but also enables functionalities that rigid electronics cannot provide. Soft electronics have demonstrated significant potentials in a wide range of applications, including skin-attachable electronics [4–6], implantable prosthetic devices [7, 8], and personalized healthcare systems [9, 10]. The unique biotic/abiotic interfacing capability of these devices ensures their stable conformal contact with human skin, resulting in exceptional sensing accuracies and signal-to-noise ratios that exceed those of traditional rigid electronics [11].

Springer

Among various components of soft electronic systems, including sensors [12, 13], actuators [14, 15], logic devices [16, 17], memory devices [18, 19], and energy storage/harvesting devices [20, 21], the light-emitting devices play a crucial role [22, 23]. Although conventional light-emitting devices have achieved significant improvement in electroluminescence (EL) performance, their inherent rigidity limits their facile integration into soft electronics. Consequently, research focus has shifted towards the development of light-emitting devices that can freely change their shapes [24]. These devices, being inherently soft, can emit light while conforming to various shape surfaces and adapting to dynamically changing environments.

The versatility of deformable light-emitting devices makes them suitable for a broad range of optoelectronic applications. One significant application is in information displays for mobile electronic devices/systems, serving as the standard human–machine interface [25]. These displays enable real-time visualization of external signals, facilitating communication between machines and users. While current mobile displays are rigid and heavy, the next generation is expected to be soft and lightweight, allowing for seamless integration with curved surfaces of the human body. Additionally, deformable light-emitting devices are finding new applications in healthcare [26]. Technologies like pulse oximetry and photomedicine, which rely on light for biosensing and treatment, benefit from the minimal invasiveness and low side effects of these devices. Deformable light sources are particularly valuable as they can significantly enhance light delivery efficiency to targeted tissues through stable, seamless interfacing, supporting the potential for long-term, point-of-care treatments.

Advances in Deformable Quantum Dot Light-Emitting Diodes

The key to developing deformable light-emitting devices lies in selecting appropriate materials and device structures that ensure both high performance and inherent softness [27]. Traditional EL devices, such as liquid crystal displays (LCDs) commonly used in commercial applications, may not be suitable for deformable EL devices due to their reliance on backlighting panels, which contribute to considerable device thickness and rigidity. Since thinner devices experience less strain under mechanical deformation, EL devices with slim profiles are required for stable operation even under significant mechanical stress. In this context, organic light-emitting diodes (OLEDs) were initially explored for deformable EL devices due to their slim profiles [28]. However, the need for higher colour purity has prompted further research into alternative EL technologies [29].

Quantum dot light-emitting diodes (QLEDs) have demonstrated their potential as ideal candidates for deformable EL devices [30–32]. Quantum dots (QDs) are colloidal semiconducting nanocrystals approximately 10 nm in size, exhibiting unique material properties such as facile colour tunability, high colour purity, and high photoluminescence quantum yield (PLQY) [33–35]. Like OLEDs, QLEDs benefit from their soft and thin form factors. The total thickness of the active layers—which includes two electrodes, charge transport layers (CTL), and the emitting layer (EML)—is typically less than 500 nm. Furthermore, given the need to reduce encapsulation thickness to minimize overall device thickness, the superior oxygen and moisture stability of inorganic light-emitters compared to organic emitters stands out as a distinct advantage of QLEDs.

Based on these advantages, extensive research efforts have focused on developing deformable QLEDs. To our knowledge, the first deformable QLEDs was reported in 2011 (Fig. 1(i)) [36]. Kim et al. fabricated a prototype of full-colour active-matrix QLED displays on flexible polyethylene naphthalate (PEN) substrates, successfully demonstrating the potential of this technology. The device can maintain its luminance under bending with a radius of curvature of 3 cm. Since then, the past decade has seen numerous proof-of-concept studies of deformable QLEDs, leading to innovations in new device form factors and enhanced EL performance (Table 1). Various unconventional soft substrates, such as adhesive tapes, papers, and elastomers, have been used to fabricate deformable QLEDs (Fig. 1ii) [37]. Also, with the advancement of device fabrication technologies, the minimum bending radius of the device has been dramatically reduced to tens of micrometers, enabling random crumpling of ultrathin devices (Fig. 1iii, iv, v) [38–40] and the controlled folding of devices for 3D origami (Fig. 1vi) [11]. Unconventional form factors, such as the fiber-type QLEDs for integrated textile electronics (Fig. 1vii) [41], and intrinsically stretchable QLEDs (Fig. 1viii) [42], have been also reported. The ultimate aim of this technology is to achieve a "free-form QLED" that can change shape freely without compromising performance.

This review article provides an overview of recent progress in deformable QLEDs, with a particular emphasis on material/device engineering and device fabrication strategies (Fig. 2). First, we examine advancements in deformable QLEDs in terms of their EL performance, focusing on light-emitting materials (I). Then, we discuss three types of device structures: bottom-emission, top-emission, and fully transparent QLEDs, highlighting materials used for soft substrates and transparent electrodes (II). We also introduce high-resolution patterning methods for QD thin films, which are essential for the fabrication of full-colour deformable QLEDs (III). Furthermore, we explore the latest studies on proof-of-concept deformable QLEDs with unconventional form factors, including flexible, foldable, fiber-type, and stretchable QLEDs (IV). Detailed materials and fabrication
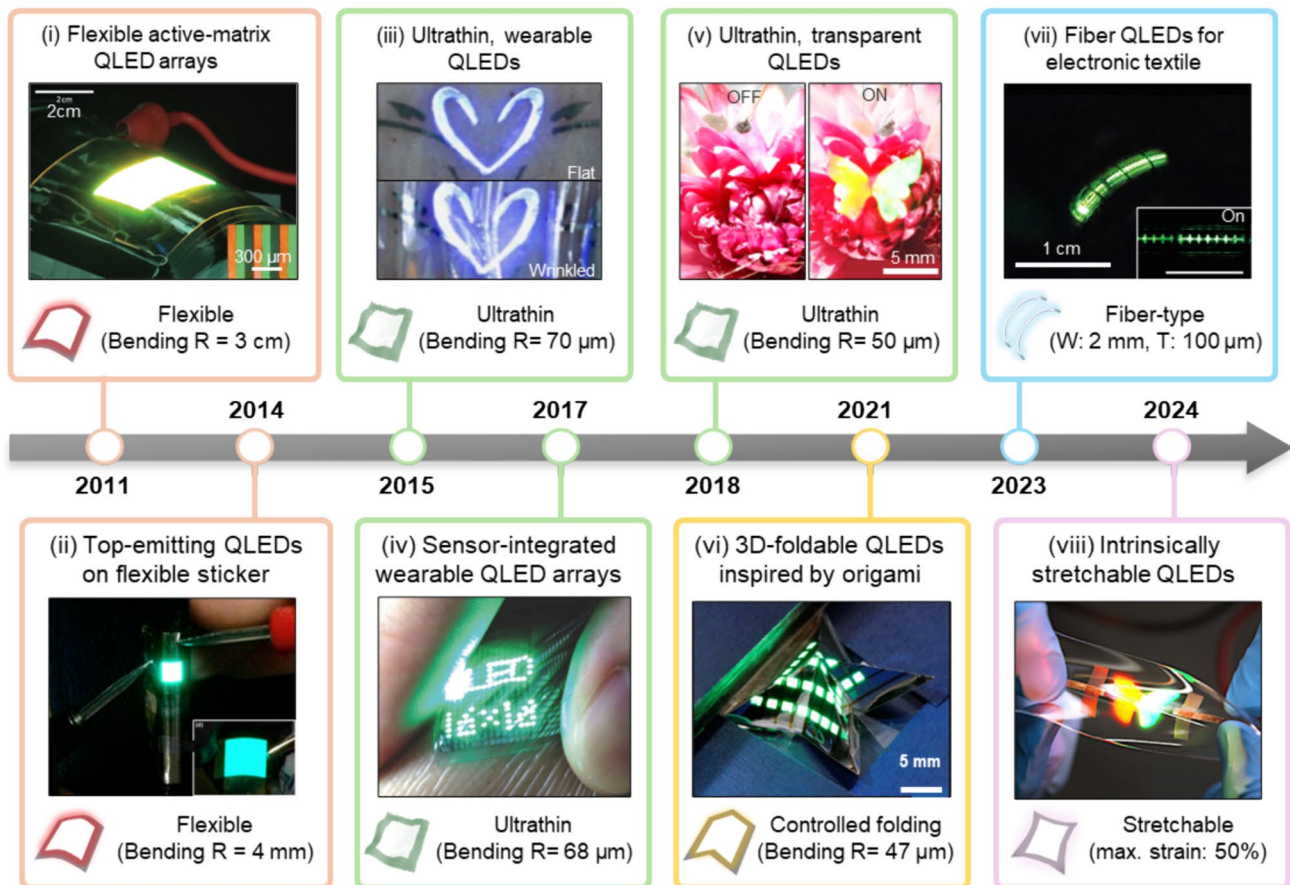
Advances in QLED form factors

Fig. 1 A brief chronology of the evolution of deformable QLEDs. "Bending R" refers to the radius of curvature of the device. For fiber-type QLEDs, "W" and "T" refers to the width and the thickness of the device, respectively. (i) Reproduced with permission from Ref. [36], Copyright 2011, Springer Nature. (ii) Reproduced with permission from Ref. [37], Copyright 2014, American Chemical Society. (iii) Reproduced with permission from Ref. [38], Copyright 2015, Springer Nature. (iv) Reproduced with permission from Ref. [39], Copyright 2017, Wiley–VCH GmbH. (v) Reproduced with permission from Ref. [40], Copyright 2018, Wiley–VCH GmbH. (vi) Reproduced with permission from Ref. [11], Copyright 2021, Springer Nature. (vii) Reproduced with permission from Ref. [41], Copyright 2023, American Association for the Advancement of Science (AAAS). (viii) Reproduced with permission from Ref. [42], Copyright 2024, Springer Nature

strategies for each form factor are discussed. Latest studies on the potential applications of deformable QLEDs, including information displays and biomedical light sources are then introduced (V). The review concludes with a brief outlook on future technologies and the remaining challenges.

Material and Device Engineering Strategies for Deformable QLEDs

Light-Emitting Materials for Deformable QLEDs

Since the Alivisatos group reported the first prototype of QLEDs in 1994, device performance has undergone significant enhancements, reaching levels comparable to those of OLEDs [43]. Recent advancements have pushed the external quantum efficiencies (EQEs) of the state-of-the-art QLEDs to approach the theoretical limits imposed by photon out-coupling [31]. These improvements stem from ongoing optimizations in material synthesis and device architectures, grounded in a deeper understanding of QLED operation, such as charge/energy transfer mechanisms at QD/CTL interfaces, exciton dynamics, and photon out-coupling processes [44]. This section reviews the performance improvement of deformable QLEDs, focusing on three representative types of colloidal QDs, including CdSe QDs, InP QDs, and perovskite QDs.

QDs for EL devices generally have a core–shell structure, which effectively confines injected electrons and holes, facilitating efficient exciton recombination. Among various

Table 1 The information about the previously-reported deformable QLEDs, including light-emitting materials, form factors, substrates, device structures, direction of light-emission, emission wavelength, maximum EQE, and maximum luminance, are summarized

Year	Light-emitting materials	Form factor (Substrate)	Normal/Inverted structure	Direction of emission	Max EQE (%)	Max luminance (cd/m^2)	Ref
2011	CdSe QDs	Flexible (PEN)	Normal	Bottom	~1.0 cd/A	N/A	[36]
2013	InP/ZnSe/ZnS QDs	Flexible (PEN)	Normal	Bottom	1.0 cd/A	640	[139]
2014	CdSe/ZnS QDs	Flexible (PI)	Inverted	Top	4	20,000	[37]
2015	CdSe/ZnS QDs	Ultrathin (Parylene/Epoxy)	Normal	Bottom	2.4	14,000	[38]
2015	CdSe QDs	Ultrathin (Epoxy)	Normal	Bottom	~2.4	~1800	[81]
2016	CdSe/CdS/ZnS QDs	Flexible (PI)	Inverted	bottom	2.7	795	[140]
2017	CdSe/ZnS QDs	Ultrathin (PET)	Inverted	bottom	8.4	50,560	[141]
2017	CdSe/CdS/ZnS QDs	Ultratthin (PET)	Inverted	Bottom	14.1	54,795	[69]
2017	CdSe/ZnS QDs	Ultrathin (Parylene/Epoxy)	Normal	Transparent	10	73,000	[40]
2017	MAPbBr$_3$ QDs	Flexible (Polymer/AgNW)	Normal	bottom	2.6	1000	[142]
2017	CdSe/ZnS QDs	Ultrathin (Parylene/Epoxy)	Normal	Bottom	~1.6	44,719	[39]
2017	CdSe/ZnS QDs	Stretchable designs (PEN)	Normal	Bottom	1.8	1,240	[125]
2018	CdZnSeS QDs	Flexible (PEN)	Normal	Bottom	10.5	76,320	[143]
2018	CdSe/CdS/ZnS QDs	Ultrathin (PI)	Inverted	bottom	24.1	~1000	[144]
2018	CdSe/ZnS QDs	Flexible (PET)	Inverted	Bottom	13.7	35,860	[145]
2018	CdSe/ZnS/CdZnS QDs	Flexible (PEN)	Inverted	Bottom	8.2	20,000	[146]
2019	ZnCdSeS QDs	Flexible (PET)	Normal	Bottom	6.7	14,880	[147]
2019	InP/ZnSe/ZnS QDs	Flexible (PET)	Inverted	Bottom	3.9	6881	[148]
2020	InP/ZnSeS QDs	Flexible (PET)	Normal	Bottom	0.9	1593	[149]
2020	CsPbBr$_3$ QDs	Flexible (PU)	Normal	Transparent	0.3	381	[150]
2020	CsPb(I/Br)$_3$ QDs	Fiber (PET)	Normal	Bottom	~1.7 cd/A	~100	[110]
2021	CdSe/ZnS QDs	Foldable (Parylene/Epoxy)	Normal	Bottom	7.9	50,513	[11]
2021	CdSe/CdZnS QDs	Stretchable designs (PI)	Inverted	Top	14.7	18,641	[123]
2022	CdSe/ZnS QDs	Ultrathin (PEN)	Inverted	Top	21.8	~80,000	[65]
2022	CdSe/ZnCdSe/ZnS QDs	Flexible (PET)	Normal	Bottom	18.6	77,060	[151]
2022	CdSe/ZnS/ZnS QDs	Flexible (PET/PMMA)	Inverted	Bottom	9.9	31,340	[78]
2022	CdSe/CdZnS/ZnS QDs	Flexible (PET)	Normal	Bottom	4.2	63,000	[152]
2022	CsPbBr$_3$ QDs	Ultrathin (Parylene/Epoxy)	Normal	Bottom	6.2	~1000	[70]
2022	CsPbI$_3$ QDs	Flexible (PET)	Normal	Bottom	12.7	362	[153]
2022	CdSe/ZnS QDs	Stretchable designs (PDMS)	Normal	Bottom	N/A	~12,000	[122]
2023	CsPbBI$_3$ QDs	Flexible (Label/PMMA)	Inverted	Top	14.3	3615	[66]
2023	CsPbI$_3$ QDs	Flexible (Paper/PMMA)	Inverted	Top	8.5	1330	[154]
2023	CdSe QDs	Fiber (PET)	Normal	Bottom	~0.1	482	[41]
2023	InP/ZnSe/ZnS QDs	Flexible (Al foil)	Inverted	Top	3.6 cd/A	40,000	[155]
2024	CdSe/ZnS QDs	Intrinsically stretchable (UV-curable PUA)	Normal	Bottom	1.2	15,170	[42]

types of QDs, CdSe QDs represent the most mature technology. Figure 3a illustrates the typical structure of a CdSe QD, featuring a CdSe core encased in ZnCdS and ZnS shells with larger bandgaps. These Cd-based QDs achieve nearly 100% PLQY and exhibit high stability against external stimuli. By adjusting the core size, Cd-based QDs can span most of the visible spectrum, as shown in Fig. 3b [45].

The EL performance of CdSe-QLEDs has seen great advancements in recent years, achieving remarkable efficiency and stability across the entire visible (RGB) spectrum range. Notably, recent studies on QLEDs utilizing red-emitting CdSe QDs have reported a high EQE of 35.6% and an exceptional lifetime (T_{95} at 1000 cd m^{-2}) over 40,000 h, underscoring the high potential for commercialization of this technology [46]. This success is attributed to the sophisticated engineering of QD nanostructures, which incorporate a mixed-crystallographic structure of wurtzite and zinc blende phases. The wurtzite phase enhances
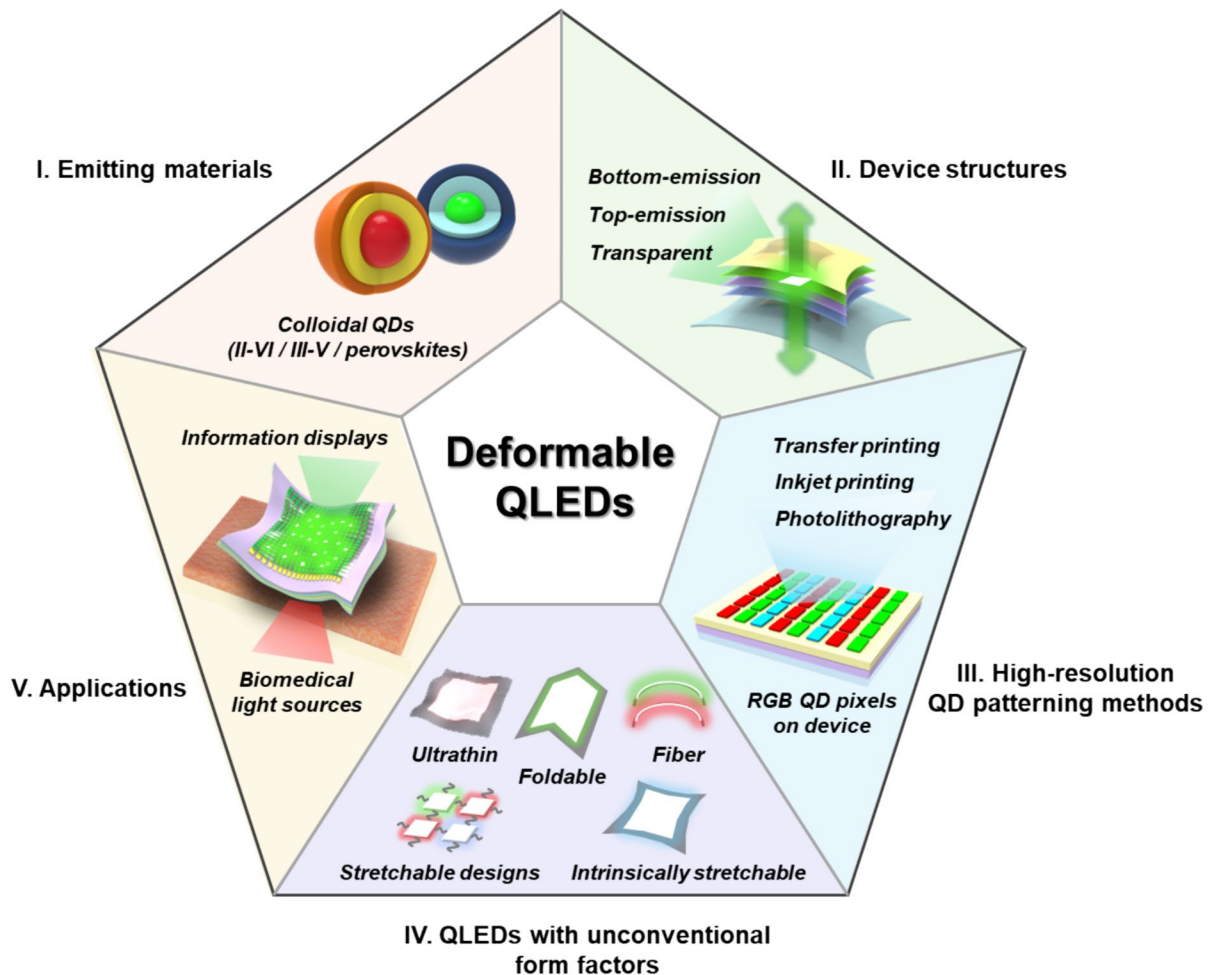
Fig. 2 Schematic overview of the development of deformable QLEDs, especially focusing on material/device engineering and fabrication strategies. Reproduced with permission from Ref. [156], Copyright 2023, Korea Flexible & Printed Electronics Society

dipole–dipole interactions that align the quantum dots in solution-processed films, while the zinc blende phase facilitates directional light emission. These features collectively improve photon out-coupling without compromising the internal quantum efficiency of the devices.

While CdSe QDs hold great promise for EL devices, the toxicity of Cd presents a significant challenge. The Restriction of Hazardous Substances (RoHS) regulations, which limit the production and sale of electronic devices containing heavy metals, have impeded the commercialization of CdSe QDs. Consequently, there has been growing interest in developing heavy-metal-free QDs to replace CdSe QDs. Among these alternatives, InP QDs have emerged as notable materials for EL devices. Figure 3c shows the general structure of an InP QD, which typically includes an InP core covered by ZnSeS and ZnS shells. Compared to CdSe QDs, there is a lattice mismatch between the Group III–V InP core and the Group II–VI ZnS shells. This mismatch leads to surface traps that reduce the PL quantum efficiency of InP

QDs. Additionally, the high covalent nature of InP makes them more susceptible to oxidation. Oxidized species are considered as structural defects of QDs as they have different unit cell structures with the original lattice. These characteristics have been significant drawbacks, resulting in the performance of InP-based QLEDs being inferior to CdSe-based QLEDs. Various synthetic strategies for InP QDs have been explored to overcome these limitations. Recently, Won et al. reported a high-performance red-emitting InP QLED with an EQE of 21.4% and a maximum brightness of 100,000 nits [47]. This was achieved through methods such as in-situ etching of the oxide surface on InP with hydrofluoric acid, effectively suppressing Auger recombination.

Adjusting the size of the InP core allows for tuning the emission wavelength. However, it remains challenging to achieve deep blue wavelengths below 450 nm (Fig. 3d) [47]. Implementing blue-emitting InP QDs requires an extremely small QD core (< 2 nm), which tends to have more crystal defects that can degrade luminescent properties, thus
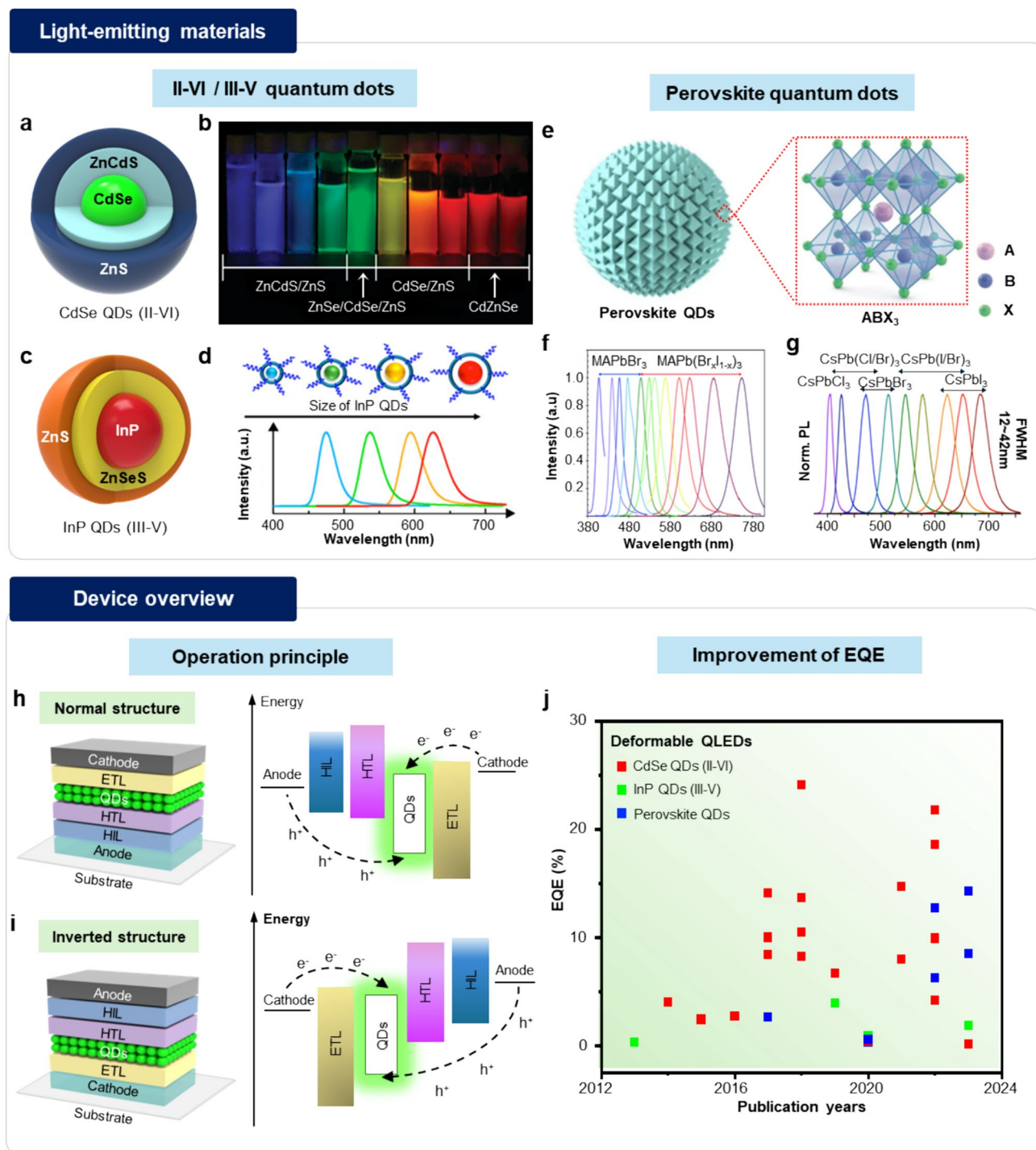
Fig. 3 Light-emitting materials and device overview of deformable QLEDs. **a** Schematic illustration of a core/shell structure for CdSe QDs. **b** PL image of Cd-based QDs with different bandgaps. Reproduced with permission from Ref. [45], Copyright 2009, American Chemical Society. **c** Schematic illustration of a core/shell structure for InP QDs. **d** Schematic illustration of InP QDs with different particle sizes and emission wavelengths. Reproduced with permission from Ref. [157], Copyright 2020, American Chemical Society. **e** Schematic illustration of a perovskite QD and its crystalline structure. Reproduced with permission from Ref. [49], Copyright 2019, American Chemical Society. Reproduced with permission from Ref. [31], Copyright 2023, Wiley–VCH GmbH (inset). **f** PL spectra of MAPbX$_3$ perovskite QDs with different bandgaps. Reproduced with permission from Ref. [50], Copyright 2015, American Chemical Society. **g** PL spectra of CsPbX$_3$ perovskite QDs with different bandgaps. Reproduced with permission from Ref. [51], Copyright 2015, American Chemical Society. **h** Schematic illustration of device structure (left) and energy band diagram (right) of QLEDs with normal structure. **i** Schematic illustration of device structure (left) and energy band diagram (right) of QLEDs with inverted structure. **j** Annual improvements in the EQE of the reported deformable QLEDs

necessitating improved synthetic strategies. As an alternative material for blue-emitting heavy-metal-free QDs, ZnSe QDs have been emerged. Recent studies by Kim et al. reported a high-performance blue-emitting QLEDs based on ZnTeSe/ZnSe/ZnS QDs, exhibiting a brightness of ~ 88,900 cd/m² and an EQE of 20.2% [48]. This high performance was achieved by replacing oleic acid ligands into chlorides, balancing charge injection by facilitating hole transport to QDs. However, deformable QLEDs based on ZnSe QDs have not been reported, as the performance and stability of blue-emitting ZnSe QLEDs are still lower than those based on CdSe or InP QDs.

Perovskite QDs have gained significant attention as emerging EL materials, due to their unique optoelectronic properties, such as a high PLQY of nearly 100%, uniform emission wavelength regardless of the particle size, and extremely narrow emission spectra (full-width at half-maximum (FWHM) < 20 nm). Figure 3e shows the perovskite QD's crystal structure, with the chemical formula of ABX_3 [31, 49]. In general, A cations are in 12-fold cuboctahedral coordination and B cations are in sixfold octahedral coordination, surrounded by X anions. For B cations, Pb^{2+} has been widely adopted for optoelectronic devices due to their high environmental stability. Depending on the ion used in the A position within the crystal structure, perovskites can be broadly divided into two groups: organic–inorganic hybrid perovskites (OHIPs) and all-inorganic perovskites. While OHIPs contain organic cations, such as methyl ammonium ions, for their A cations, all-inorganic perovskites contain metallic cations, mostly Cs^{2+}. For both types of perovskites, emission wavelengths can be tuned by exchanging anions. When the size of anions increases, the bandgap of perovskites decreases, exhibiting a red-shift of the PL emission (Fig. 3f and g) [50, 51].

While 3D bulk perovskites have small exciton binding energy, resulting in inefficient exciton recombination, perovskite QDs have higher exciton binding energy due to the quantum confinement effect [52, 53]. This characteristic makes perovskite QDs promising for EL devices. Recently, the performance of LEDs utilizing perovskite QDs has seen significant advancements. The keys to the fabrication of high-performance perovskite QLEDs lie in managing surface defects and reinforcing carrier confinement. Various strategies have been explored, such as ion doping, ligand exchange, and shell coating. Recently, by reacting with benzylphosphonic acid (BPA), 3D bulk perovskite films were converted into perovskite QDs with a core/shell structure, leading to effective carrier confinement. Additionally, the phosphonic acid group in BPA passivated surface traps [54]. As a result, the perovskite QLEDs exhibited a high brightness of ~ 470,000 cd m⁻², and an EQE of 28.9%. However, the toxicity of lead ions in perovskite QDs remains a challenge. Efforts to develop lead-free perovskite QLEDs are ongoing, but their stability is considerably lower than that of lead-containing perovskite QLEDs, requiring further research and development.

Operation Principle and Performance of Deformable QLEDs

The device structure of the first-reported QLED was simple, featuring a four-layered configuration of indium tin oxide (ITO)/p-type semiconducting polymers (p-paraphenylene vinylene, PPV)/CdSe QDs/Mg. The device exhibited light emission of ~ 100 cd m⁻² under forward bias. To address the large band energy offset between the electrodes and QDs, it is crucial to establish stepwise pathways for charge carriers to achieve efficient carrier injection into QDs. Thus, researchers introduced charge transport layers (CTLs) between the QDs and electrodes, which significantly enhanced the device EL performance by facilitating efficient charge injection to the QDs. Initially, organic semiconductors were used for both hole transport layers (HTLs) and electron transport layers (ETLs). Since Bulovic group reported the potential of inorganic ETLs, however, the combination of organic HTLs and inorganic ETLs has proven to be the standard for high-performance QLEDs [55]. Solution-processed inorganic materials, such as ZnO or ZnMgO nanoparticles, have become the preferred materials for ETLs due to their high electron mobility and stability.

The operation principle of QLEDs can be largely categorized into two: a normal structure (Fig. 3h) and an inverted structure (Fig. 3i). The typical configuration of a normal-structured QLED consists of substrate/anode/hole injection layer (HIL)/HTL/QDs/electron transport layer (ETL)/cathode, while the inverted structure generally has a configuration of substrate/cathode/ETL/QDs/HTL/HIL/anode. When an electrical bias is applied, charge carriers are injected into the QDs by passing through the CTLs. For example, electrons from the cathode transport through the ETL, while holes move from the anode through the HIL and HTL. Additionally, CTLs can function as charge-blocking layers for the opposite carriers, aiding in efficient exciton formation. ETL materials with deep highest occupied molecular orbital (HOMO) levels and HTL materials with high-lying lowest unoccupied molecular orbital (LUMO) levels possess hole-blocking and electron-blocking properties, respectively.

The key criteria for the selection of CTL materials are carrier mobility, band alignment, and deposition methods. While most state-of-the-art QLEDs utilize ZnO or ZnMgO nanoparticles for their ETLs [56], the selection of materials for HIL and HTL remains variable, particularly depending on the device structure. For normal structures, semiconducting poly(3,4-ethylenedioxythiophene) (PEDOT:PSS), has been widely used for HIL. For HTL, a semiconducting polymer, poly[(9,9-dioctylfluorenyl-2,7-diyl)-co-(4,4′-(N-(4-

s-butylphenyl)diphenylamine)] (TFB) [57], is the most preferred choice due to its high hole mobility. Other conjugated polymers, such as poly(9-vinylcarbazole) (PVK) [58] and poly[N,N'-bis(4-butylphenyl)-N,N'-bis(phenyl)-benzidine] (poly-TPD) [59], have also been used in some reports [60]. These polymers are generally solution-processable and are applied using spin-coating to form thin films. For solvent orthogonality, octane is the most preferred choice for QD solvents, minimizing damage to the underlying HTLs.

For inverted structures, vacuum-deposited semiconducting materials are often used for the HTL and HIL. This is because conjugated polymers are typically dissolved in organic solvents, which may cause damage the QD layer when applied to upper layers. In this regard, various small-molecule organic semiconductors, including tris(4-carbazoyl-9-ylphenyl)amine (TCTA) [61, 62], or 4,4′-Bis(N-carbazolyl)-1,1′-biphenyl (CBP) [63], are vacuum-deposited for HTLs. For efficient hole injection from the metallic anodes, a molybdenum oxide (MoO_x) overlayer has been widely used [64]. The performance of QLEDs with an inverted structure is comparable to that of conventional normal-structured QLEDs.

Based on rapid innovations in material engineering strategies for both QDs and CTLs, the EL performance of QLEDs has undergone significant enhancements. In parallel, the performance of deformable QLEDs has also dramatically improved. Figure 3j shows the increasing trends of EQE in deformable QLEDs over the past decade. CdSe QDs have been the most widely used light-emitting materials for deformable QLEDs due to their high EL performance and stability. For instance, Yu et al. reported flexible top-emitting QLEDs based on CdSe QDs, exhibiting a maximum EQE of 21.8%, and a maximum luminance exceeding 80,000 cd m^{-2} [65]. Recently, deformable QLEDs utilizing InP QDs and perovskite QDs have also been reported. In 2023, Qin et al. reported flexible perovskite QLEDs fabricated on disposable substrates, achieving a maximum EQE of 14.3%, the highest record for flexible perovskite QLEDs [66].

Despite these advances, a performance disparity persists between rigid and deformable QLEDs. This gap is mostly attributed to the constraints in the manufacturing process due to the relatively low thermal/chemical resistance of soft plastic substrates compared to the conventional rigid substrates. Low-temperature fabrication processes may lead to degraded crystallinity of the thin-film materials, including electrodes and CTLs, causing inefficient charge transport. Additionally, thin films deposited on soft substrates may not possess sufficient uniformity comparable to those on rigid substrates, leading to unfavourable charge transport pathways within the device. The insufficient protectability of soft thin encapsulation layers against the external environment can also degrade the performance and stability of deformable QLEDs. Therefore, enhancing the performance of deformable QLEDs necessitates further advancements not only in the active layers, such as QDs and CTLs, but also in the soft substrates and encapsulation layers.

Device Structures of Deformable QLEDs

The EQE of LEDs is defined as the product of internal quantum efficiency (IQE) and photon out-coupling efficiency. Thus, it is crucial to enhance the efficiency of extracting photons from the device to increase the EQE. Various approaches, including microcavities [67, 68], various micro- or nanostructures, microlenses [69], directional emission, have been reported to enhance photon out-coupling efficiency. Photons generated from QDs are emitted from the device through the transparent electrodes, so at least one of the top or bottom electrodes must be sufficiently transparent. Depending on the position of the transparent electrodes, the device structure can be broadly categorized into three groups: bottom-emitting, top-emitting, and fully transparent QLEDs. In this section, we review these representative structures of deformable QLEDs, with a particular focus on the transparent electrodes on soft substrates.

Bottom-Emitting QLEDs

Figure 4a shows the general structure of bottom-emitting deformable QLEDs. To fabricate bottom-emitting QLEDs, transparent bottom electrodes should first be deposited on soft transparent substrates. Following the subsequent coating of active layers, including CTLs and QDs, reflective metallic electrodes are deposited on top. While rigid bottom-emitting QLEDs are generally fabricated on glass substrates, bottom-emitting deformable QLEDs require transparent plastic substrates. Polymers such as polyethylene terephthalate (PET), polyethylene naphthalate (PEN), colorless polyimide (cPI), and epoxy resin are widely used for transparent substrates. Free-standing thin films of these polymers exhibit high transparency, surface uniformity, and good interfacial adhesion between the substrates and electrodes. Additionally, these polymers possess sufficient thermal and chemical resistance to withstand QLED fabrication processes, which involve solution-processing and thermal annealing. Some polymers, especially elastomers like polydimethylsiloxane (PDMS) and polyurethane (PU), require additional treatments for surface planarization to make them suitable for device fabrication.

Selecting proper materials for bottom transparent electrodes is also a critical issue for bottom-emitting deformable QLEDs Various transparent conductors have been reported. For conventional rigid QLEDs, ITO, a transparent conducting oxide, has been the most widely used electrode material due to its outstanding transparency and conductivity. In general, the harsh sputtering process of ITO restricts its
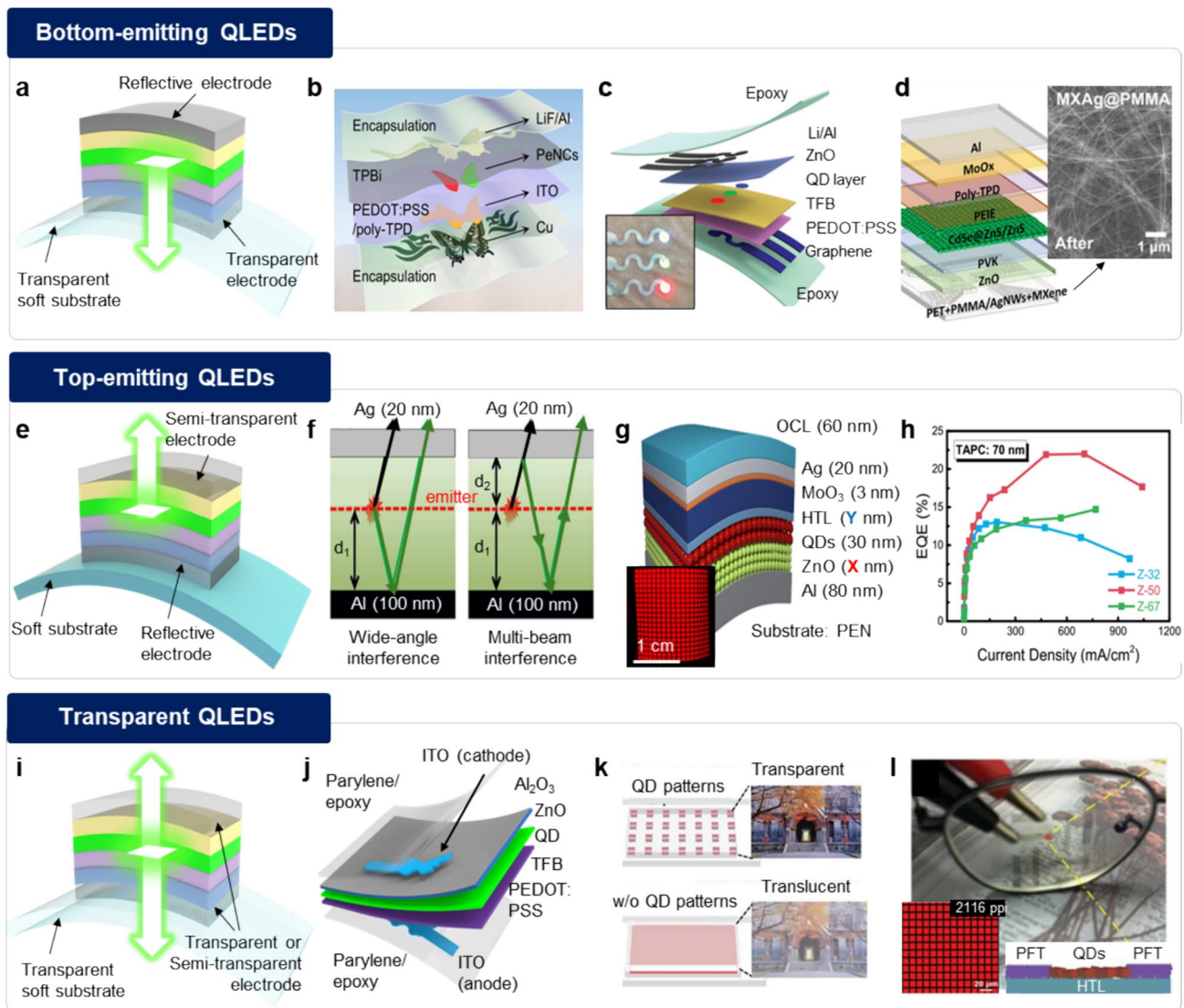
Fig. 4 Representative device structures of deformable QLEDs. **a** Schematic illustration of the device structure of bottom-emitting QLEDs. **b** Schematic illustration for exploded view of flexible QLED with ITO bottom electrode. Reproduced with permission from Ref. [70], Copyright 2022, American Association for the Advancement of Science (AAAS). **c** Schematic illustration for exploded view of flexible QLED with graphene bottom electrode. Inset image shows the device operation. Reproduced with permission from Ref. [81], Copyright 2015, Wiley–VCH GmbH. **d** Schematic illustration (left) and cross-sectional TEM image (right) for exploded view of flexible QLED with silver nanowire/MXene bottom electrode. Reproduced with permission from Ref. [78], Copyright 2022, American Chemical Society. **e** Schematic illustration of the device structure of top-emitting QLEDs. **f** Microcavity effect in top-emitting QLEDs, including wide-angle interference (left) and multi-beam interference (right). Reproduced with permission from Ref. [68], Copyright 2016, American Chemical Society. **g** Schematic illustration of top-emitting flexible QLED, with semi-transparent top electrode. Inset shows the image of large-area flexible QLED arrays. **h** Enhanced EQE of top-emitting QLEDs due to the microcavity effect. Reproduced with permission from Ref. [65], Copyright 2022, American Chemical Society. **i** Schematic illustration of the device structure of fully-transparent QLEDs. **j** Schematic illustration for exploded view of flexible and transparent QLEDs. Reproduced with permission from Ref. [40], Copyright 2018, Wiley–VCH GmbH. **k** Comparison between the transparency of devices with QD patterns (top) or without QD patterns (bottom). **l** Images of the fully transparent QLED. The left inset shows the patterned QD pixels, while the right inset is a schematic image of the cross-sectional structure of the device that designed to prevent direct contact between the HTL and ETL. Reproduced with permission from Ref. [85], Copyright 2023, Wiley–VCH GmbH

deposition on active layers to prevent the plasma damage to underlaying layers. Despite its rigid and brittle nature, ITO has been applied to bottom-emitting deformable QLEDs with special layer designs that manage induced strain. For instance, Kwon et al. reported ultrathin bottom-emitting perovskite QLEDs, utilizing ITO as transparent bottom electrodes [70]. ITO was directly deposited onto parylene/epoxy double layers (Fig. 4b). When the thicknesses of the top

encapsulation and bottom substrate are designed to be equal, the ITO is located on the neutral mechanical plane, experiencing minimal bending-induced strains. Consequently, ITO can maintain its electrical properties despite various deformations such as bending, wrinkling, or crumpling.

However, the long-term mechanical stability of brittle ITO electrodes is controversial, as fatigue accumulates during repeated deformations. Micro-sized cracks propagate through the crystalline structures, leading to the gradual degradation of conductivity. In this regard, various transparent conductors with inherently soft mechanical properties have been studied. Considering critical factors such as conductivity, transparency, flexibility, work function, surface uniformity, and their fabrication process, low-dimensional conductors like silver nanowire (Ag NW, 1D) network [71–73], graphene (2D) [74–77], and MXene (2D) network [78–80] have shown potential for soft, transparent electrodes.

Choi et al. reported the fabrication of ultrathin bottom-emitting QLEDs based on graphene electrodes (Fig. 4c) [81]. Graphene was patterned and transfer-printed onto a flexible parylene/epoxy resin substrate. The transfer printing was repeated multiple times with precise alignment to fabricate multi-layered graphene, achieving sufficient conductivity. The surface of graphene is highly smooth and possesses a work function deep enough to enable efficient hole injection to adjacent HIL. Composites of 1D and 2D materials have also been reported. Jiang et al. demonstrated the fabrication of flexible bottom-emitting QLEDs based on hybrid transparent electrodes of MXene and Ag NWs (Fig. 4d) [78]. The hybrid transparent electrode consists of a highly conductive Ag NW network mixed with solution-processed MXene flakes, directly spray-coated onto flexible PET substrates. The wire-to-wire junctions of the percolated Ag NW network were welded with MXene flakes, achieving a low sheet resistance of ~ 13.9 Ω sq^{-1} and a high transparency of 83.8%. The composite of 1D and 2D conductors was embedded in a buffer layer of poly(methyl methacrylate) (PMMA), achieving smooth surface of electrodes favourable for subsequent solution processing (i.e., spin coating).

Top-Emitting QLEDs

Due to the easy fabrication process and high EL performance, the majority of reported QLEDs are based on bottom-emitting structures. However, these structures face challenges when it comes to the fabrication of high-resolution active-matrix (AM) displays. In AM-QLED arrays, QLED pixels need to be fabricated on top of backplanes that include arrays of thin film transistors (TFTs) and wiring interconnections. Since a substantial portion of the total area is covered by the opaque TFTs and interconnections in the backplane, bottom-emitting QLEDs have a limited emission area. Such

a low aperture ratio is a critical limitation when fabricating high-resolution displays.

To address this issue, top-emitting device structures have been studied. Since the light emission in a top-emitting structure is directed opposite to the backplane, the device can have a larger emission area. Figure 4e illustrates the general structure of top-emitting deformable QLEDs. Reflective electrodes, typically composed of 80–100 nm thick metal films, are deposited on soft substrates. Not only can transparent plastic substrates be used, but also various opaque flexible substrates such as papers or metal foils can be employed, along with proper surface treatments or deposition of planarization layers. For the top electrodes, a thin metal film (less than 20 nm) of Ag or MgAg alloys is commonly used, deposited via vacuum deposition processes. The thickness of the top electrodes must be optimized to balance conductivity and transparency.

Another advantage of top-emitting deformable QLEDs is their significantly improved light-extraction efficiency. In bottom-emitting QLEDs, a considerable number of generated photons are lost due to the bottom substrates (i.e., substrate mode) and the transparent electrodes (i.e., waveguide mode), because of total internal reflection of light. These optical modes trap photons within the device, preventing a substantial portion of photons from being emitted outwards, reducing the overall device efficiency. Consequently, the light-extraction efficiency of QLED is generally less than 20%. Top-emitting QLEDs, on the other hand, are designed to emit light from the top surface of the device. This design eliminates the presence of the substrate and the highly refractive transparent electrodes in the light emission pathways, leading to higher light-extraction efficiency.

Additionally, the unique structure, where emitters are placed between a reflective bottom electrode and a semi-transparent top electrode, enhances the light-extraction efficiency by the microcavity effect. This structure can be optically treated as a Fabry–Perot cavity [82]. By optimizing the cavity length (i.e., thickness of each layer), light reflected from the bottom and top electrodes interferes constructively, resulting in enhanced electroluminescent (EL) emission with narrower spectra. Within the cavity, two types of interference can occur (Fig. 4f) [68]. Wide-angle interference occurs between light directly emitted from QDs and light reflected from the bottom electrode with the same wavevector. Multiple-beam interference, on the other hand, occurs when light bounces back and forth between two electrodes. For wide-angle interference, the distance between the emitter and the bottom reflective electrode (d_1) determines the resonant wavelength. For multiple-beam interference, the thickness of the entire functional layers ($d_1 + d_2$) is crucial. If the resonant wavelength matches the emitter's PL wavelength, enhanced emission through constructive interference is achieved. Otherwise, the emitter's intrinsic emission is

suppressed due to destructive interference. Thus, the cavity length must be precisely optimized to meet the resonant conditions.

Due to these advantages of top-emitting structures, extensive research has been dedicated to the development of top-emitting QLEDs. Yu et al. reported the fabrication of large-area, top-emitting QLED passive-matrix (PM) arrays on a flexible PEN substrate (Fig. 4g) [65]. The device is based on an inverted structure, featuring a layered configuration of bottom cathodes/ETL/QDs/HTL/HIL/top anodes. An 80-nm-thick reflective Al film was used for the bottom cathode, while a 20 nm-thick semi-transparent Ag film was used for the top anode. To achieve uniform coating over a large area, blade coating was used instead of spin coating for the layers. A surfactant-added solution was employed to ensure uniform coating. Additionally, the thicknesses of the ZnO layers and the organic HTL were adjusted to fully exploit the microcavity effect. The device exhibited the highest maximum EQE when the thicknesses of the ZnO and HTL were 50 nm and 60 nm, respectively (Fig. 4h).

Fully Transparent QLEDs

Transparent displays are considered key technologies for next-generation electronics, playing a crucial role in augmented reality (AR), wearable electronics, and Internet of Things (IoTs) [83]. Their transparency significantly broadens potential applications of EL devices by allowing visual information to be displayed on objects without altering their original appearance and functionality [84]. The conventional approach to fabricating transparent displays focuses on maintaining a high aperture ratio, thus minimizing the emission area of each pixel. However, the decrease in efficiency and brightness with reduced emission area remains a challenge. Consequently, research has shifted towards increasing the transparency of the pixels themselves, and fully transparent QLEDs with transparent conductors applied to both the top and bottom electrodes have been reported.

The key factors for fabricating transparent QLEDs lie in the selection of top transparent electrodes. Various transparent conductors, including thin metal films, ITO, graphene, and Ag NWs, have been used for top transparent electrodes. For instance, Choi et al. reported the fabrication of ultrathin, transparent QLEDs utilizing ITO for both electrodes [40]. The device exhibited high brightness (bottom: 43,000 cd/m^2 at 9 V) and excellent transmittance (90% at 550 nm, 84% over the visible range). To minimize sputtering damage during ITO deposition, an Al$_2$O$_3$ protective layer was deposited on top of the ZnO layers. The combination of ZnO/Al$_2$O$_3$ layers effectively protects the underlying layers from plasma damage during ITO sputtering. Additionally, the insulating nature of Al$_2$O$_3$ limits the electron injection and thus balances

the charge injections to the QDs, achieving high QLED performance. All active layers, including the two brittle ITO electrodes, were positioned in the neutral mechanical plane of the device, allowing stable operation even under harsh mechanical deformations.

Another approach to enhancing the transparency of QLEDs is micro-patterning the QD EMLs. Utilizing this method, Luo et al. reported the fabrication of highly transparent QLEDs [85]. By creating void spaces between each micropattern of QDs, the transparency of the device could be increased. However, in high-resolution QLEDs, these void spaces between pixels are highly susceptible to leakage current due to direct contact between the HTL and ETL. To address this issue, the authors developed novel strategies to pattern QDs based on electrostatic force-induced deposition. The leakage current caused by the void spaces between pixels is significantly suppressed by substrate-assisted insulating perfluorooctyl trichlorosilane (PFT) patterns. Using this approach, high-resolution QD patterns could be achieved (2,116 ppi), and the resulting QLEDs exhibited a high maximum EQE of 15.6% and a high transparency of 91% over the visible range.

High-Resolution QD Patterning Methods for Full-Color QLEDs

Full-color deformable QLEDs hold significant promise for various human-friendly display applications, such as virtual reality (VR) displays [86], portable displays, and skin-attachable wearable displays [39, 70, 87]. As the distance between the display device and the human eyes decreases, obtaining clear images necessitates higher resolution with smaller pixel sizes. For instance, a 75-inch 4 K Ultra-high-definition (4 K UHD, 3840×1080) television screen has a pixel size of approximately 430 μm, resulting in about 58 pixels-per-inch (ppi). In contrast, a 6.2-inch 4 K UHD mobile display necessitates a much smaller pixel size of 30 μm, which is about 833 ppi. Consequently, there is a growing need to develop a reliable QD patterning process capable of achieving micro-patterns of QDs in the range of tens of micrometers or less. Furthermore, minimizing damage to the QDs and the underlying active layer during the patterning process is crucial for EL device applications. Harsh etching processes during patterning are thus undesirable. In this section, we introduce three representative QD patterning methods: transfer printing, inkjet printing, and photolithography. All patterning methods introduced in this section are designed to minimize damage to the QDs and underlying layers, ensuring their suitability for practical application of deformable QLEDs.

Transfer Printing

Transfer printing refers to a deposition technique in which a thin film, initially coated on a donor substrate, is transferred onto a target substrate [36, 38, 88]. In general, an elastomeric stamp, consisting of silicone elastomer, is used to detach and transfer the film. The detachment and transfer occur due to differences in interfacial adhesion between the film, the stamp, and the substrate [89, 90]. To facilitate the film detaching and transfer process, various methods such as the aid of self-assembled monolayer (SAM) [91], kinetic control, thermal control, and laser ablation have been reported to manipulate the interfacial adhesions.

Transfer printing technique based on the stamping process has several advantages in device fabrication. First, it does not require the involvement of water or other organic solvents for film detachment, making it suitable for transferring films that are sensitive to solvents. Additionally, the transfer printing technique is often useful in the fabrication of soft electronic devices. Most soft plastics cannot withstand high temperatures, so high-temperature deposition or annealing processes are carried out on a donor substrate, such as a wafer, and then the film is subsequently transferred.

Extensive research has been conducted on high-resolution QD patterning via transfer printing. The initial approach utilizes a structured elastomeric stamp. A significant milestone in the history of deformable QLEDs was reported by Kim et al., who reported the fabrication of full-color flexible AM-QLED arrays using structured stamping [36]. This process begins by rapidly picking up QDs coated on a donor substrate with a structured stamp. To facilitate easy detachment from the donor substrate, a self-assembled monolayer (SAM) of silane molecules is coated on the wafer. A structured stamp with specific protruding patterns is prepared by pouring PDMS onto the surface-treated mold. During the rapid pick-up process, with a peeling speed of ~ 70 mm/s, the surface energy of the PDMS stamp, being slightly lower than that of the donor substrate, aids in retrieving QD films from the donor substrate. Subsequently, by contacting the inked stamp to the device stack and slowly peeling back the stamp at 1 mm/s, QDs with desired patterns are transferred onto the target substrate. Using this technique, the authors successfully fabricated a 4-inch full-color AM-QLED array, demonstrating the potential of this technology (Fig. 5b). QLEDs were fabricated on a hafnium-indium-zinc oxide (HIZO) TFT backplane with an array size of 320×240, achieving a high resolution of 100 ppi. Each RGB pixel has an emissive area of 46 μm × 96 μm.

While the structured stamping technique enables a simple and highly reliable patterning process for the full-color QLED array fabrication, issues arise as device resolution increases. When pixel size decreases, the transfer yields of structured stamping degrade dramatically, with significant losses at the edges of patterns. To address this issue, Choi et al. developed an intaglio transfer printing technique [38]. The intaglio transfer printing process involves the following three steps: (1) rapidly picking up QDs from the donor substrate using an elastomeric stamp with a smooth surface, (2) contacting the inked stamp with intaglio trenches engraved with patterns and slowly peeling off, and (3) transferring the patterned QDs remaining on the PDMS stamp to the target substrate. Using the intaglio transfer technique, a small pixel size of 5 μm was successfully transferred, with sharp edges.

Recently, researchers have further improved the intaglio transfer printing technique. Kwon et al. reported the fabrication of high-resolution, full-color wearable perovskite LEDs, using advanced intaglio transfer. Researchers introduced an organic layer of a 2,2′,2″-(1,3,5-benzinetriyl)-tris(1-phenyl-1-H-benzimidazole) (TPBi) on top of the perovskite QD layers. TPBi plays a crucial role in preventing the delamination of perovskite QDs during the pick-up process. Also, the low adhesion between the PDMS stamp and TPBi resulted in the easy releasing from the stamp. In this regard, perovskite QDs were able to detach from the intaglio trench without being damage, and TPBi was removed with methyl acetate. Using this technique, they achieved a high resolution (~ 2,550 ppi) of RGB perovskite QD patterns with nearly 100% of transfer yields (Fig. 5d). Such technique was readily applied to the fabrication of full color, wearable perovskite QLEDs, exhibiting high performance (EQE ~ 6.2%) and outstanding stability during harsh mechanical deformation.

Inkjet Printing

Inkjet printing operates on the principle of ejecting ink droplets through nozzles located in the print head, with droplets precisely directed to specific locations on the target substrate as programmed [92]. To achieve uniformly printed patterns, various factors such as the composition of inks, rheological properties of solvents, volume of each droplet, printing speed, nozzle size, and temperature condition must be carefully optimized [93]. Compared to the transfer printing process, inkjet printing is more cost-effective, with a higher deposition rate and minimized waste of QDs. This makes it particularly valuable for industrial applications, including the mass production of display devices. Consequently, extensive research has been devoted to developing inkjet printing techniques to achieve high-resolution QD patterns over large areas.

The key to inkjet printing technology lies in the design of the inks, as many parameters, such as drying speeds and wettability, can be significantly affected by the ink composition. Yang et al. introduced an optimized design of QD inks for printing high-resolution arrays of QD patterns and applied this method to fabricate QLEDs (Fig. 5e) [94]. The droplets, ejected from a piezo-driven print head, are printed onto the
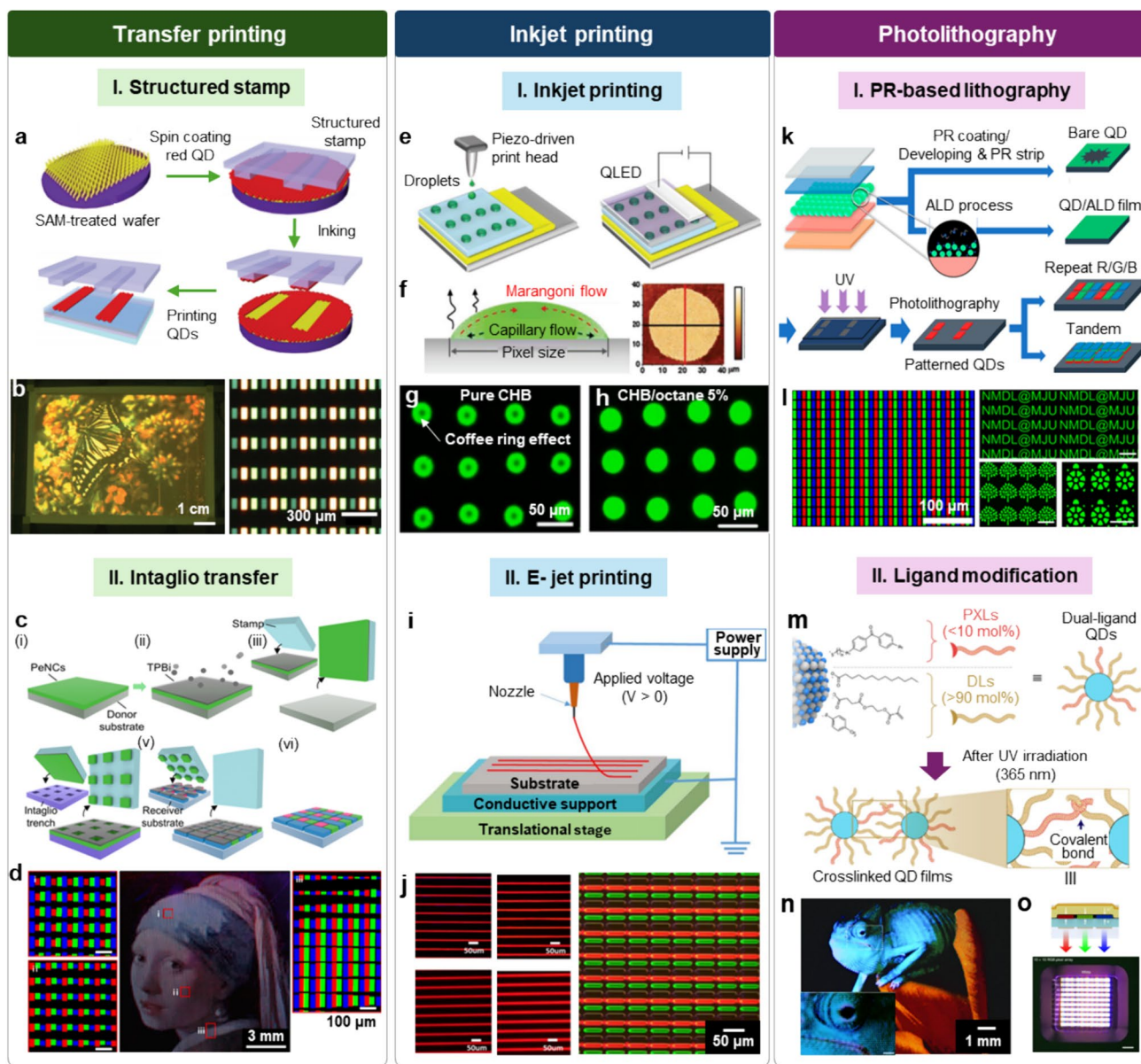
Fig. 5 Representative methods for high-resolution QD patterning compatible with full-color EL device applications. **a** Schematic illustration of the transfer printing process using structured stamp. **b** Photograph of a 4-inch full-color QD display (left) and optical microscopy image showing concurrent RGB EL from active pixels (right). Reproduced with permission from Ref. [36], Copyright 2011, Springer Nature. **c** Schematic illustration of the intaglio transfer printing process of perovskite QDs using TPBi organic layer. **d** PL images of the transfer printed RGB patterns of perovskite QDs, depicting "Girl with a Pearl Earring". Left and right PL images show magnified views of specific regions. Reproduced with permission from Ref. [70], Copyright 2022, American Association for the Advancement of Science (AAAS). **e** Schematic illustration of the inkjet printing process. **f** Schematic illustration of the pixel drying process (left) and atomic force microscope (AFM) image of uniformly printed QD pixel. **g**, **h** PL images of printed QD pixels. QD ink containing pure CHB solvent exhibits coffee-ring effect (**g**), while inks containing CHB with 5% octane result in uniform pixel (**h**). Reproduced with permission from Ref. [94], Copyright 2020, Wiley–VCH GmbH. **i** Schematic illustration of the E-jet printing process. **j** Fluorescence image of the patterned lines at different printing speed (left images). PL image of the multi-color (R/G) QD pixels with 500 ppi (right). Reproduced with permission from Ref. [98], Copyright 2023, Royal Society of Chemistry. **k** Schematic illustration of the QD patterning via PR-based lithography and ALD process. **l** PL image of RGB QD patterns with 800 ppi (left), and various images and letters obtained by sequential photolithography process (right). All scale bars indicate 100 μm. Reproduced with permission from Ref. [101], Copyright 2021, American Chemical Society. **m** Schematic illustration of a ligand-assisted direct photolithography. **n** PL image of the RGB QD patterns with a delicate pixel design. **o** Schematic illustration (top) and image (bottom) of the full-colour QLED with RGB QD pixels, patterned via direct lithography. Reproduced with permission from Ref. [104], Copyright 2022, Springer Nature

surface of the HTL, a poly-TPD layer. The primary challenge in high-resolution inkjet printing is producing single, small droplets that dry into uniform pixels. A common issue with inkjet printing is the non-uniform morphology of printed patterns, such as the "coffee ring effect," where ink accumulates more at the edges than in the center [95]. To address this, researchers proposed using inks composed of mixtures of octane and cyclohexylbenzene (CHB) to improve pixel quality. While formulations with 0% to 10% octane are suitable for printing, using pure CHB as a solvent results in coffee ring stains at the edges due to capillary flow (Fig. 5g). By mixing 5% octane with 95% CHB, Marangoni flow is induced towards the center, effectively reducing the coffee ring effect and achieving a nearly uniform QD distribution across the pixel (Fig. 5f and h). This approach enabled the production of high-quality pixel arrays with a resolution of 500 ppi, meeting the requirements for 8 K displays. The inkjet printing technique was successfully applied to the fabrication of QLEDs, which exhibited a maximum luminance of approximately 3000 cd m^{-2}.

On the other hand, the electrohydrodynamic printing method, also known as E-jet printing, has emerged as a promising alternative to conventional piezo-driven inkjet printing due to its capability of printing higher resolution patterns [96, 97]. E-jet printing operates by applying voltage to a conductive nozzle, creating an electric field between the nozzle and the substrate (Fig. 5i) [98]. This method offers significant advantages over traditional piezo-electric inkjet printing, allowing for much higher resolution through the control of ink viscosity under the influence of the electric field. Wang et al. utilized E-jet printing to create high-resolution QD pixel arrays exceeding 500 ppi and applied this technique to the fabrication of QLEDs. Voltage was applied between the nozzle and the substrate, and line width was fine-tuned according to the printing speed. Figure 5j illustrates variations in line width at different printing speeds with the same ink viscosity, showing smooth edges at 6.7 μm, 9.7 μm, 13.1 μm, and 18.1 μm for speeds of 7 mm s^{-1}, 5 mm s^{-1}, 3 mm s^{-1}, and 1 mm s^{-1}, respectively. This indicates that increasing the printing speed results in narrower lines. Consequently, the bottom emission QLEDs with a pixel density of 500 ppi were fabricated, exhibiting a maximal current efficiency of 14.4 cd A^{-1}.

Photolithography

Photolithography has been the most mature technology in semiconductor device fabrication [99]. Based on its high technological maturity, research has been conducted to pattern QDs, utilizing ultraviolet (UV)-sensitive photoresist (PR), photomasks, and developers [100]. However, the conventional photolithography may not be suitable for the fabrication of EL devices, as it involves subsequent

solution processing process, including the spin-coating of PR, developing, solvent washing, and removing residual PR. Since QD films and underlying active layers are vulnerable to solvent attacks, the performance of the device can be degraded after the photolithographical patterning of QDs.

To overcome this issue, researchers have focused on enhancing the solvent resistance of QDs. For example, Kim et al. reported an advanced lithographic process that employs atomic layer deposition (ALD) to create a protective layer for QDs against solvent attacks (Fig. 5k) [101]. By reacting the surface of QD films with a diethylzinc (DEZ) precursor, a thin film (~ 20 nm) of ZnO overlayer was coated on the QD layers. Due to the high reactivity between DEZ and the ligands of QDs, typically oleic acid and oleylamine, either ligand exchange occurs, or DEZ gets attached between the pre-existing organic ligands. Consequently, QD films exhibit strong resistance to external solvents, allowing PR to be directly coated on top of the QDs. After UV exposure on photomasks, QDs in the unexposed regions are removed by solvent washing, resulting in high-resolution patterning of QD pixels. By repeating the same lithography process, R/G/B (800 ppi) tri-color QD patterns, various images, and text were patterned on the substrate (Fig. 5l).

Although previous studies have reported the facile patterning of QDs using conventional photolithography, the fundamental limitations of the approach involving PR have yet to be resolved. For example, incomplete removal of PR residue can lead to uneven charge injection within devices. Also, the use of PR or protective layers may degrade the PL properties of QDs, resulting in the deterioration of the EL performance [102]. Recently, an alternative method to pattern QDs via lithography has been reported that excludes the use of PR [103]. Hahm et al. introduced CdSe QDs capped with dual ligands, consisting of photo-crosslinkable ligands (PXLs, < 10 mol%) and dispersing ligands (DLs, > 90 mol%) (Fig. 5m) [104]. While DLs play a crucial role in forming a stabilized QD dispersion in solvents, PXLs form covalent bonds with adjacent ligands in response to UV irradiation. By selectively exposing the dual-ligand QD films to UV light, only the QDs in the unexposed region are removed by developing the films with proper solvents. Using this method, researchers could achieve the direct patterning of QDs with outstanding resolution and high throughput. Figure 5n demonstrates a fluorescence image of high-resolution RGB QD patterns achieved via direct photolithography, with a maximum resolution reported up to 15,000 ppi. This technique was readily applied to the fabrication of full-color QLED arrays (Fig. 5o), showing significant potential for optoelectronic device applications.

Deformable QLEDs with Unconventional Form Factors

Research focus in QLED development have traditionally been on enhancing the EL performance and stability of QLEDs. Through advancements in QD synthesis and a deeper understanding on device operation mechanism, significant improvements have been made in both performance and stability [105, 106]. However, the advent of new information technologies, such as the IoTs, artificial intelligence, and data science, has shifted the research trends from conventional rigid electronics to soft electronics, aiming for enhanced integration between machines and humans. Consequently, there has been a growing demand for the development of deformable QLEDs, leading to extensive research in this area [24]. The high performance, stability, and ultrathin nature of QLEDs make them highly compatible with deformable EL device applications. In this section, we highlight new fabrication approaches used to create QLEDs with unusual form factors, including flexible, foldable, fiber-type, and stretchable QLEDs. Since most components of QLEDs, including electrodes and various inorganic/organic materials, are inherently rigid, the main research focus here has been on how to maintain stable device performance when QLEDs are mechanically deformed repeatedly.

Non-stretchable Types (Flexible, Foldable, and Fiber-Type) of Deformable QLEDs

Downscaling the device thickness is one of the most effective approaches to achieve flexibility of the device, even when the device is composed of rigid materials [107, 108]. In general, a solid material has critical parameters associated with its capability of bending: the critical bending radius and critical thickness. The critical bending radius is the minimum radius at which the solid maintains its operation while bent, and the critical thickness is the required thickness for bending to a given radius. As a brief approximation, the surface strain (S) of a thin-film material with thickness (h) and bending radius (R) can be expressed as $S = h/2R$. Therefore, by reducing the material thickness, the surface strain can be lowered, reducing the critical bending radius. In other words, if the device thickness is below its critical thickness, it can bend to a given radius without failures, regardless of the rigidity of the materials involved.

Additionally, the utilization of a neutral mechanical plane that balances tensile and compressive strains is another strategy to enhance the mechanical stability of devices during bending. The position of this plane can be determined based on the thickness and stiffness of each layer in the device. Layers farther from this plane may experience more strain, increasing the risk of device failure. Therefore, creating an extremely thin structure and placing the stiffest layers near the neutral mechanical plane can improve device stability.

Based on these approaches for efficient strain management, the bending radius of flexible QLEDs has dramatically decreased from the initial few centimeters to tens of micrometers. For example, Choi et al. demonstrated an ultrathin wearable RGB QLED that can be freely deformed with a small radius of curvature (~ 70 μm) [38]. The device is very thin, measuring around 2.6 μm in total thickness (Fig. 6(a)), with double encapsulation layer of parylene-epoxy (~ 1.1 μm) and active layer (~ 300 nm). To ensure the stability of these ultrathin QLEDs, they used double encapsulation where epoxy (SU-8) acted as protective barrier for parylene during ITO sputtering and external damage. Positioning of active layer at neutral mechanical plane was done to reduce bending stress on stiff ITO layer (Fig. 6b). With this ultrathin design, the fabricated electronic tattoo could easily bend and conform to curved surfaces while maintaining stable performance even when wrinkled or crumpled (Fig. 6c). This devices achieved high brightness levels, reaching up to 14,000 cd/m^2 at 7 V with EQE of 2.35% (Fig. 6d).

A few years later, researchers further improved this strain management technique and achieved the 3D origami of ultrathin QLEDs through a precisely controlled folding deformation. The principle behind foldable devices is that when a specific region of the device is thinner than the adjacent areas, most of the deformation is concentrated in that thinner region. Typically, thickness differences are created through patterning processes like lithography. The greater the thickness difference, the smaller the bending radius, resulting in a sharper fold of the device. Therefore, the two key challenges in developing foldable QLEDs are: (i) how to generate thinner region without damaging the underlying active layer, and (ii) how to manage the strain concentrated at the crease where most deformation occurs.

To address these issues, researchers developed new pre-programming techniques for crease generation. Kim et al. used a selective laser-programmed etching method (Fig. 6e) to pre-program hinges for three-dimensional foldable QLEDs [11]. In this approach, a 100-nm-thick Ag etch stop layer was introduced to protect the underlying active layers from damage during the encapsulation etching process. By adjusting the laser intensity, they enabled the selective etching of only the top epoxy overcoating while precisely producing folding lines (Fig. 6f). Additionally, since the active layers in the crease region are located near the neutral mechanical plane, they can endure the mechanical strain focused on the crease. Consequently, the researchers
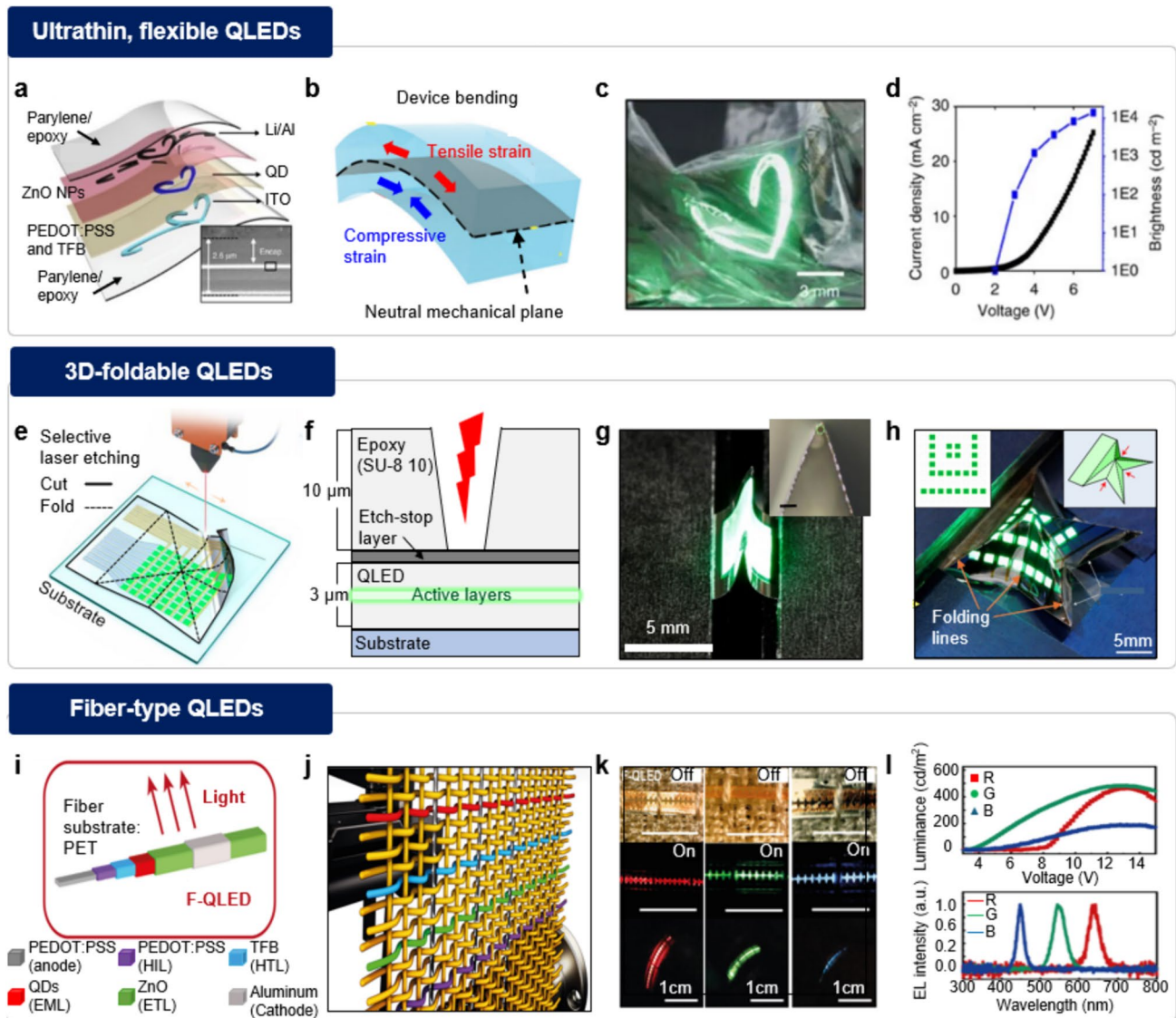
Fig. 6 Fabrication of flexible, foldable, and fiber-type QLEDs. **a** Schematic illustration for exploded view of electronic tattoo using ultrathin wearable QLEDs. Inset shows cross-sectional SEM image of the device. **b** Schematic illustration of neutral mechanical plane under bending. **c** Image of ultrathin green QLEDs on crumpled Al foil. **d** J-V-L characteristic of the device. Reproduced with permission from Ref. [38], Copyright 2015, Macmillan Publishers. **e** Schematic illustration showing the pre-programming of foldable QLEDs using selective laser etching. **f** Cross-sectional schematic illustration of the device structure. **g** Image showing sharp folding of foldable QLED with an etching depth of 10 μm. Inset shows magnified side view image of the folded device (bending radius, 0.047 mm). **h** Image of three-dimensional star-like PM QLED array. The left inset shows the pattern of the QLED array. The right inset shows the structural illustration of the device. Reproduced with permission from Ref. [11], Copyright 2021, Springer Nature. **i** Schematic illustration of F-QLED. Six functional layers are sequentially deposited on a PET fiber substrate. **j** Schematic illustration of textile electronic system. **k** Images of F-QLEDs woven in the textile for red (left), green (middle), and blue (right) emission. Scale bars, 1 cm. **l** Luminance (top) and electroluminescence (bottom) characteristics of red, green, and blue F-QLEDs. Reproduced with permission from Ref. [41], Copyright 2023, American Association for the Advancement of Science

fabricated sharply folded QLEDs with a minimum bending radius of 0.047 mm (Fig. 6g). This specially designed flexible hinge can withstand localized strain during repetitive folding, as demonstrated by consistent EL properties after enduring 500 cycles of repeated bending. This approach allows for transforming flat ultrathin QLED arrays into complex 3D shapes like airplanes, butterflies, cubes, and pyramids using techniques similar to origami (Fig. 6h).

Fiber-type QLEDs have a distinctive one-dimensional architecture that allows them to be twisted and bent in any direction [109, 110]. Unlike traditional film-type QLEDs that exhibit Lambertian emission, fiber-type QLEDs feature

a circular arrangement of layers around the central axis, emitting light in all directions. Their unique device form factors make them suitable for use in wearable optoelectronic applications, particularly electronic textiles [111]. To achieve optimal performance in these applications, it is necessary to use optimized device designs and fabrication processes that result in low driving voltage and high current efficiency.

Key factors for the fabrication of high-performance fiber-type QLEDs include the uniform coating of all component layers on the fiber substrate, including electrodes, charge transport layers (CTLs), and emissive layers (EMLs). While thermal evaporation is often used to deposit metal electrodes, solution-based processes such as dip coating and spray coating are used to deposit other functional layers of QLEDs [112, 113]. Dip coating, in particular, can offer uniform coatings by immersing the fiber in a solution and controlling the withdrawal speed. Additionally, appropriate encapsulation methods are required to protect the device from damage caused by bending or environmental factors.

Lee et al. reported the development of fiber-type quantum dot light-emitting diodes (F-QLEDs), along with other fiber-type devices such as photodetectors, field-effect transistors, and supercapacitors, all integrated into a textile electronic system (Fig. 6j) [41]. The F-QLEDs were fabricated on PET fiber substrates (2 mm width, 100 mm length, ~ 100 μm thick). The functional layers were coated using a dip coating method (Fig. 6i), and the withdrawal speed was adjusted to achieve a film with the desired thickness and smooth surface. Aluminum cathodes were deposited by thermal evaporation. In order to avoid mechanical breakdowns during automated weaving, additional PET fiber strips were employed for passivation. The F-QLEDs in red, green, and blue colors (Fig. 6k) were woven into textiles using automated weaving. The red, green, and blue-emitting QLEDs achieved peak brightness levels of 463, 482, and 188 cd/m^2, respectively, at approximately 10 V (Fig. 6l). As a proof-of-concept of this technique, researchers integrated various fiber-type devices into a single electronic textile, by weaving fibers with an automated loom. The multi-functional electronic textile can visualize external signals via F-QLEDs.

Stretchable QLEDs Based on Geometrically Designed Structures

Beyond flexibility, research is now advancing towards developing light-emitting devices with stretchable form factors, allowing displays to change shape freely [114]. These stretchable light-emitting devices, capable of maintaining their EL performance under repeated stretching, are expected to be applied to versatile applications, particularly in various human-friendly wearable electronics [115]. However, imparting stretchability to LEDs presents

more significant challenges than fabricating flexible LEDs. The common strategy effective for flexible devices, such as downscaling device thickness or employing neutral mechanical plane, may not be effective for fabricating stretchable LEDs. An alternative approach to address this issue involves using geometrically designed structures in LEDs, such as island-bridge configurations and wavy, wrinkled patterns.

Traditional QLEDs use materials such as transparent conducting oxides [116], metal thin layers, and organic or inorganic semiconductors [117–121]. These materials exhibit excellent EL performance due to their highly uniform and crystalline morphology. However, they are inherently rigid and fragile. Even minimal strain can cause severe cracks in the active layers, leading to device failure. The island-bridge design is a potential solution to maintain high EL performance while also enabling stretchability. This idea involves placing rigid LED parts on stretchable substrates. These components are connected using either geometrically stretchable (serpentine) or intrinsically stretchable metal interconnections. The stretchable interconnections play a vital role in dissipating stress throughout the system, especially in the stiff island devices, to ensure that the electrical properties are maintained even during repeated stretching.

Lee et al. developed a stretchable CdSe/ZnS QLED array integrated with strain and temperature sensors for showing bio-signals (Fig. 7a and b) [122]. The array has a strain-releasing structure where flexible QLEDs are placed on stiff islands and connected by stretchable liquid metal interconnections. This structure allows high flexibility with no optical degradation under biaxial strain of up to 30% (Fig. 7c). By shifting the stress from the stiff QLED component to the stretchable connections, this design maintain stability and functionality of the QLED devices effectively.

Kim et al. reported a stretchable sensory-neuromorphic system in which a quantum dot-based epidermal photonic actuator (Fig. 7d), an artificial synapse, and a mechanoreceptor are connected by stretchable interconnects [123]. An inverted top-emission QLED (Fig. 7e) was created using ligand-exchanged colloidal quantum dots to provide balanced electron–hole injection. By employing a sinter-free ink printing technique, they developed intrinsically stretchable interconnections composed of dynamically cross-linked polymer and Ag flakes. The connections showed high conductivity (18,550 S/cm) and stretchability (160%). The sinter-free method minimized thermal damage to the hole transporting layer (CBP) and prevented oxygen vacancy changes in the electron transporting layer (ZnO), hence improving the stability of the device. The final device, integrated on a PDMS substrate as a 5 × 5 epidermal photonic actuator (Fig. 7f), exhibited reliable functionality when subjected to crumpling and strains of up to 25% (Fig. 7g).

While there are benefits to using high-performance conventional QLED devices, there are challenges to achieving
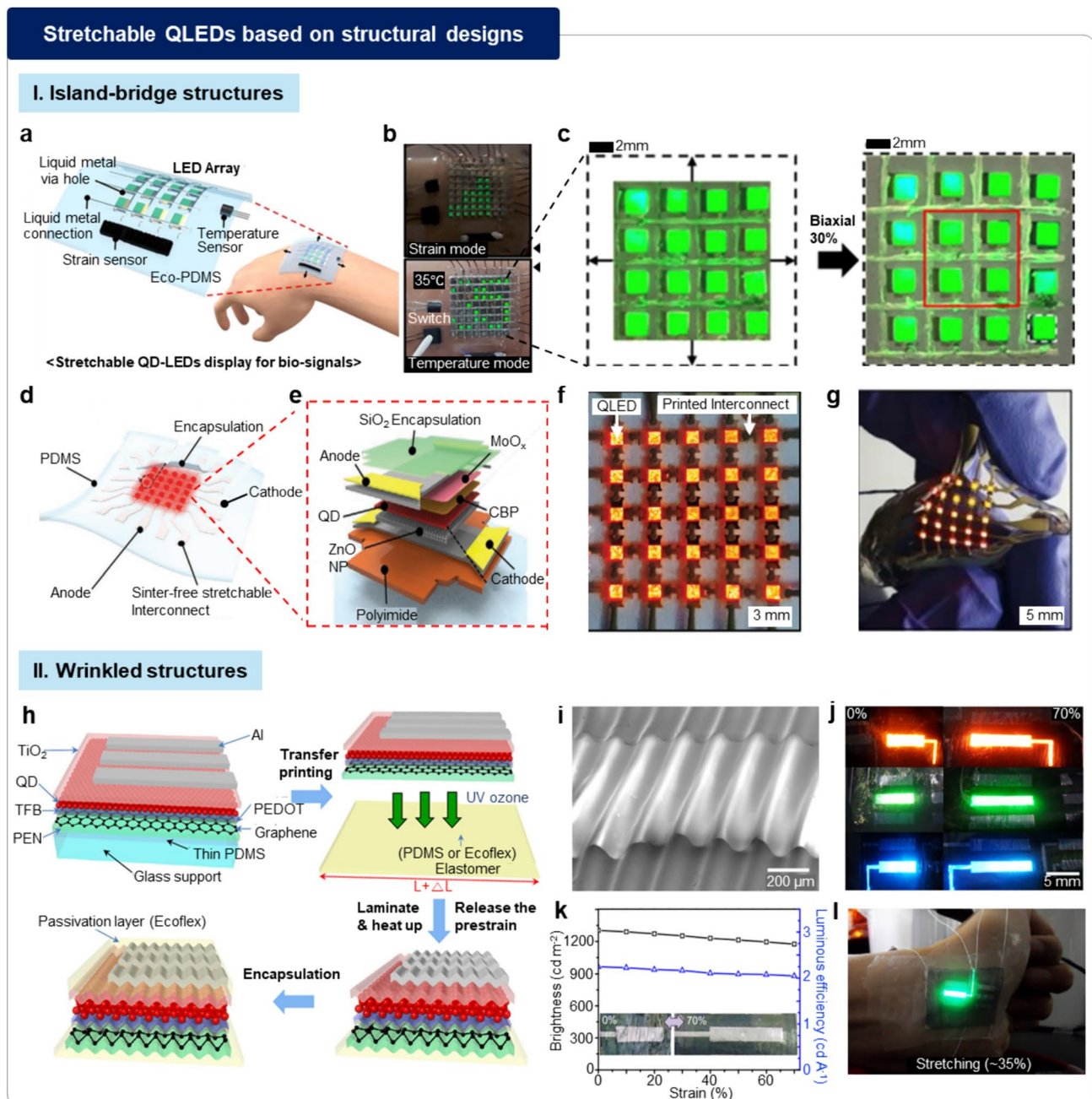
Fig. 7 Fabrication of stretchable QLEDs based on structural designs. **a** Schematic illustration of stretchable QLED array with sensors. **b** A skin-attached device displaying the applied strain (top) and the skin temperature (bottom). **c** Image of stretchable QLEDs without deformation (left) and under biaxial stretching of 30% (right). Reproduced with permission from Ref. [122], Copyright 2021, Elsevier B.V. **d** Schematic illustration of epidermal photonic actuators based on intrinsically stretchable QLEDs. **e** Schematic illustration for exploded view of the QLED devices. **f** Image of the 5×5 epidermal photonic actuator on the PDMS substrate. **g** Image of the crumpled device. Reproduced with permission from Ref. [123], Copyright 2021, Wiley–VCH GmbH. **h** Schematic illustration of the device structure and fabrication process of stretchable QLEDs with wavy configuration. **i** SEM image of a wavy LED formed by 70% pre-strain. **j** Images of the stretchable red, green, and blue QLEDs stretched up to 70%. **k** Brightness and luminous efficiency characteristics of the stretchable red QLEDs under strains up to 70%. The inset shows images of the wavy QLEDs stretched up to 70%. **l** Image of the epidermal QLEDs attached on a wrist at a driving voltage of 9 V. Reproduced with permission from Ref. [125], Copyright 2017, American Chemical Society

high resolution and fill factor. The fill factor decreases as the display stretches because stretchable interconnections expand while the rigid LED components stay fixed. Interconnections between pixels hinder progress in developing high-resolution stretchable displays.

Another approach to make ultrathin QLED devices stretchable is forming a wrinkled structure [124]. This technique includes transferring a planar ultrathin QLED onto pre-strained elastomer substrate. Upon the removal of the prestrain, the flexible LED undergoes the formation of a regular wavy buckling structure. Wavy design in this device allows it to endure stretching until wrinkles flatten, achieving flexibility without distorting the device significantly. It is important to also account for ultrathin thickness and neutral mechanical plane when designing the device structure to prevent damage during prestrain release. Additionally, forming uniform buckles with a small bending radius across device surface is crucial for higher performance.

Kim et al. reported a stretchable wavy optoelectronic sensor using colloidal QDs (Fig. 7h) [125]. They first fabricated an ultrathin QLED using a flexible graphene electrode on a PET/glass substrate. Subsequently, the device was placed on a prestrained elastomeric substrate using thermal release tape. Releasing the prestrain produced consistent wavy design (Fig. 7i), enabling necessary level of stretchability. Ecoflex layer was added to enhance durability as passivation layer. Use of wavy pattern, coupled with device structure designed to match neutral mechanical strain, successfully reduced stress during stretching. Consequently, QLEDs exhibited significant flexibility, with bending radius of 35 μm and could endure stretching up to 70% strain without affecting their EL performance (Fig. 7j). The device maintained stable operation even under the 70% of stretching, exhibiting nearly constant brightness (~ 1200 cd m^{-2}) and luminous efficiency (~ 2 cd/A) (Fig. 7k). Based on the outstanding mechanical stability, the device was readily applied to wearable electronics, attached on the wrist skin accompanying dynamic movements (Fig. 7l).

Intrinsically Stretchable QLEDs

Despite extensive studies on geometrically designed stretchable LEDs, enhancing the fill factor (i.e., the ratio of emission area to total area) and mechanical endurance of these stretchable LEDs remains challenging, hindering the commercial availability of stretchable displays. For example, stretchable displays based on serpentine interconnections experience a significant decrease in fill factor during stretching because the emission area remains fixed while the area of the interconnections continues to expand. Recent research has shifted their attention towards creating fully stretchable LEDs [42, 126]. The new strategy for fabricating these LEDs involves the integration of light-emitting materials

with intrinsically stretchable materials. Many of the previously reported intrinsically stretchable LEDs use stretchable organic light-emitting composites made of polymeric light emitters, such as SuperYellow [127, 128], and elastomers [129]. However, the performance of these devices is significantly lower than that of their rigid or flexible counterparts, exhibiting low brightness ($< 10,000$ cd m^{-2}) and high turn-on voltage (> 5–8 V). Therefore, there has been a need to develop high-performance intrinsically stretchable light-emitting devices.

Recently, a novel stretchable EML based on QD nanocomposite was reported and readily applied to the fabrication of intrinsically stretchable QLEDs [42]. Kim et al. reported a stretchable EML composite consisting of QDs, styrene-ethylene-butylene-styrene (SEBS) elastomer, and TFB (Fig. 8a). This composite enabled the development of a stretchable QLED that maintains brightness even when stretched to 50% (Fig. 8b). The internal structure of the stretchable EML features QD emitters evenly packed within the SEBS matrix, while TFB forms island-like structures at the bottom. During the uniaxial stretching process, the ternary composite film undergoes unequal compression in two distinct regions: region A, which is the TFB-island area, and region B, which is the non-island area. In region A, mostly the top QD/SEBS layer except TFB island is compressed. In region B, the entire film is fully compressed as a result of Poisson's effect (Fig. 8c). The stretchable QD composite film, which has a unique embossing structure over a TFB-rich island, exhibits a smooth surface morphology without any cracks when stretched 50%. This contrasts with bare QD films, which develop numerous microcracks under same stretching condition (Fig. 8d).

One of the main challenges in utilizing stretchable yet insulating SEBS in EML was ensuring balanced carrier injection into QDs. An optimal weight ratio of QD:SEBS:TFB = 10:1:0.5 was determined through optimization. In this case, the TFB-rich islands served as an efficient hole transport pathway from HTL to stretchable EML, thereby overcoming a significant drop in EL performance. In addition, the analysis of grazing-incidence small-angle X-ray scattering (GISAXS) shows that the horizontal and vertical interplanar distances (d_{xy} and d_z) remain nearly constant during stretching. This suggests that the density of QD particles within the stretchable EML does not change when the material is deformed (Fig. 8e).

Further engineering improvements were implemented on the remaining QLED layers in order to increase their stretchability (Fig. 8f). The stretchable anode employed PUA-embedded Ag NWs, together with a surfactant and dimethyl sulfoxide (DMSO) doped conducting PEDOT:PSS (PH1000). The stretchable cathode was fabricated by depositing Ag NW/Ag/liquid metal layers with small resistance changes under high strain using spray coating method. The
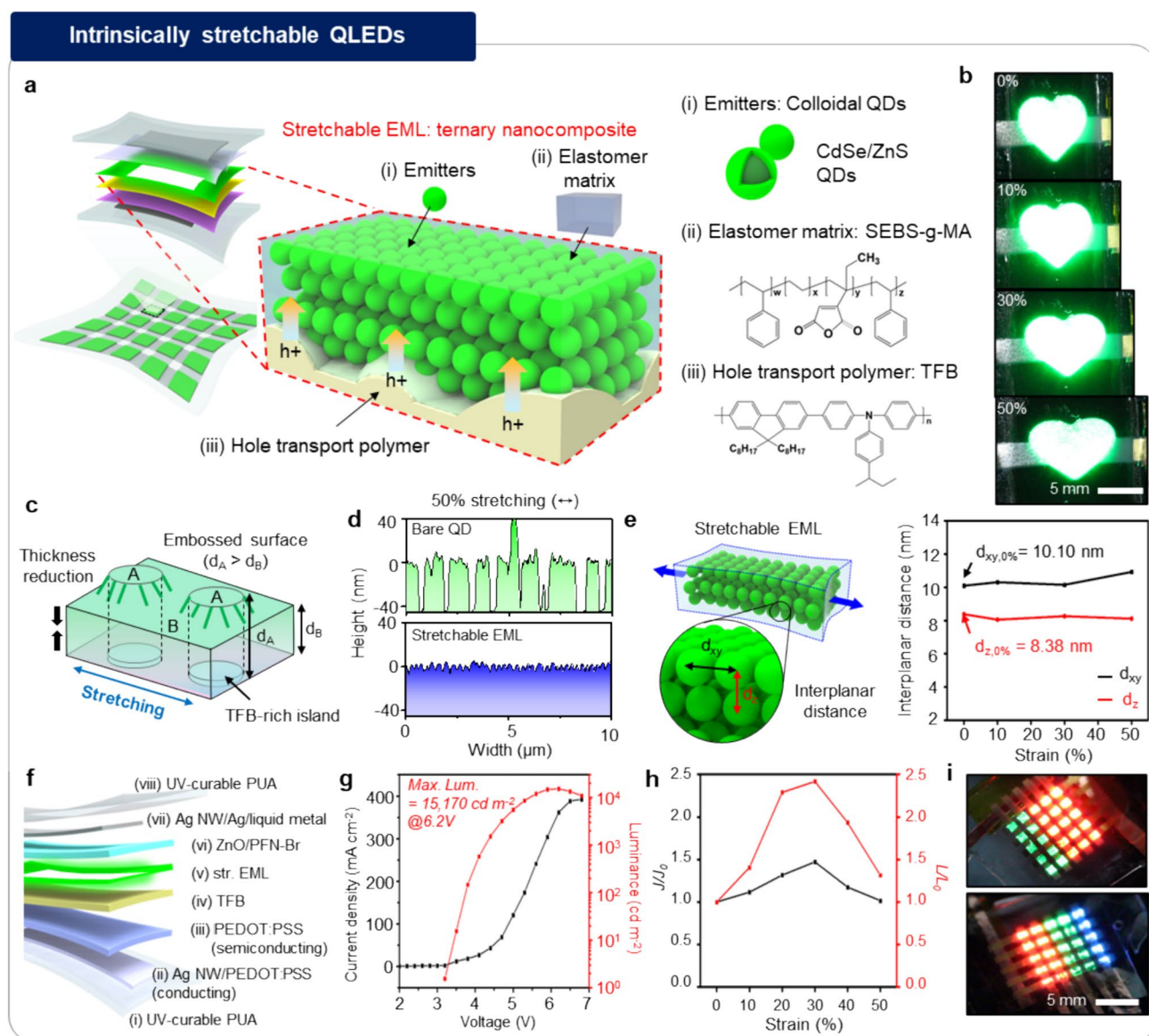
Fig. 8 Fabrication of intrinsically stretchable QLEDs. **a** Schematic illustration of stretchable EML (center) for intrinsically stretchable QLED (left). The stretchable EML is a ternary composite of QDs, SEBS-g-MA and TFB (right). **b** Images of intrinsically stretchable QLED stretched up to 50%. **c** Schematic illustration of structural change for stretchable EML ($QD_{100}S_{10}T_5$) under stretching. **d** Height profiles of the top surfaces of the stretched bare QD film (top) and stretchable EML (bottom) stretched by 50%. **e** Schematic illustra-

tion of stretchable EML (left) and interplanar distance between QDs (right) within the stretched EML. **f** Schematic exploded illustration for device structure of the intrinsically stretchable QLEDs. **g** J-V-L characteristic of the device. **h** Strain-dependent current density and luminance change under strains up to 50%. **i** Image of multicolour intrinsically stretchable PM-QLED arrays. Reproduced with permission from Ref. [42], Copyright 2024, Springer Nature

semiconducting PEDOT:PSS (AI4083) was added with a non-ionic fluorosurfactant (Capstone™ FS-31) to enhance its wettability and stretchability in the hole injection layer.

Based on this comprehensive material and design strategy, a stretchable device with a low turn-on voltage of 3.2 V and a maximum luminance of 15,170 cd/m² at 6.2 V was fabricated (Fig. 8g). They exhibited no

luminance degradation when stretched up to 50%. Surprisingly, they initially showed an increase in brightness for the first ~30% strain (Fig. 8h). Achieving a significant breakthrough, they have successfully created 5 × 5 full-color intrinsically stretchable passive matrix QLED arrays. These arrays showed high stretchability under convex, concave, and cyclic stretching deformations (Fig. 8i).

Applications of Deformable QLEDs

Information Displays Integrated with Sensors

With the successful debut of various form factor displays, such as foldable phones and rollable televisions, information displays with flexible form factors have emerged as a major trend in next-generation display development [25, 130]. These displays are not only aesthetically impressive but also offer new functionalities that traditional rigid displays cannot provide, such as the ability to freely adjust screen size and shape to suit user preferences. Based on the outstanding EL performance, stability, and color reproducibility, QLEDs can serve as the core component for deformable information displays that visualize external signals to users [39, 131].

Lee et al. demonstrated a flexible audiovisual display with a multifunctional skin-attachable sensor for monitoring UV exposure, pressure, and temperature (Fig. 9a) [132]. An 8×8 flexible QLED array was composed of stretchable and conductive materials; liquid metal as the interconnect and Au grid/PEDOT:PSS as the electrode. The Si rubber encapsulation layer provided protection against sweat and external environment. The QLED array integrated with UV sensor and temperature sensor successfully displayed the body temperature and UV exposure intensity on the wrist. Furthermore, a thin piezoelectric PVDF film acted as a speaker, emitting warning sounds when biosignals deviated from their typical ranges (Fig. 9b). This study has the potential for wearable mobile healthcare, especially in the case for elderly patients and infants who require constant health monitoring.

Recently, a prototype of an interactive wearable display was developed using deformable QLEDs capable of pressure sensing. Lee et al. developed an ultraflexible and transparent electroluminescent skin that can visualize high-resolution (> 1000 dots per inch) images of pressure distribution in real time (Fig. 9c) [133]. The transparent piezoresistive layer composed of Te-PEDOT nanowires with cellulose nanofibers, which has high sensitivity and a fast response time (< 1 ms), was in contact with top film, and the flexible QLED was fabricated on a bottom PI film. When am external pressure is applied, the top and bottom films conform to each other and form a conductive path proportional to the pressure intensity. As a result, the superfine image reflecting the exact shape and magnitude of the applied pressure can be achieved without the need for pixel structures (Fig. 9d). This study addresses the accurate visualization of pressure distribution on curved surfaces, which provides a framework for skin prostheses and robotics applications.

Kim et al. reported the development of an ultrathin, skin-attachable QLED display (~ 5.5 μm) with features of high brightness (44,719 cd m^{-2} at 9 V) and a low temperature increase during operation [39]. The 8×8 passive matrix ultrathin QLED display was integrated with driving circuits, microcontroller, temperature sensor, accelerometer, and touch sensor on a flexible printed circuit board (Fig. 9e). The skin-mounted QLED display could visualize letters, numbers, and symbols to display various information to users. The microcontroller unit processes the temperature and step count, while the touch sensor allows the users to change the sensing mode or scroll the display by inducing a change in the resistive-capacitive (RC) delay. Real-time measurement of temperature and step count was demonstrated, and the wearer could carry out mode switching and text scrolling through the interactive display (Fig. 9f).

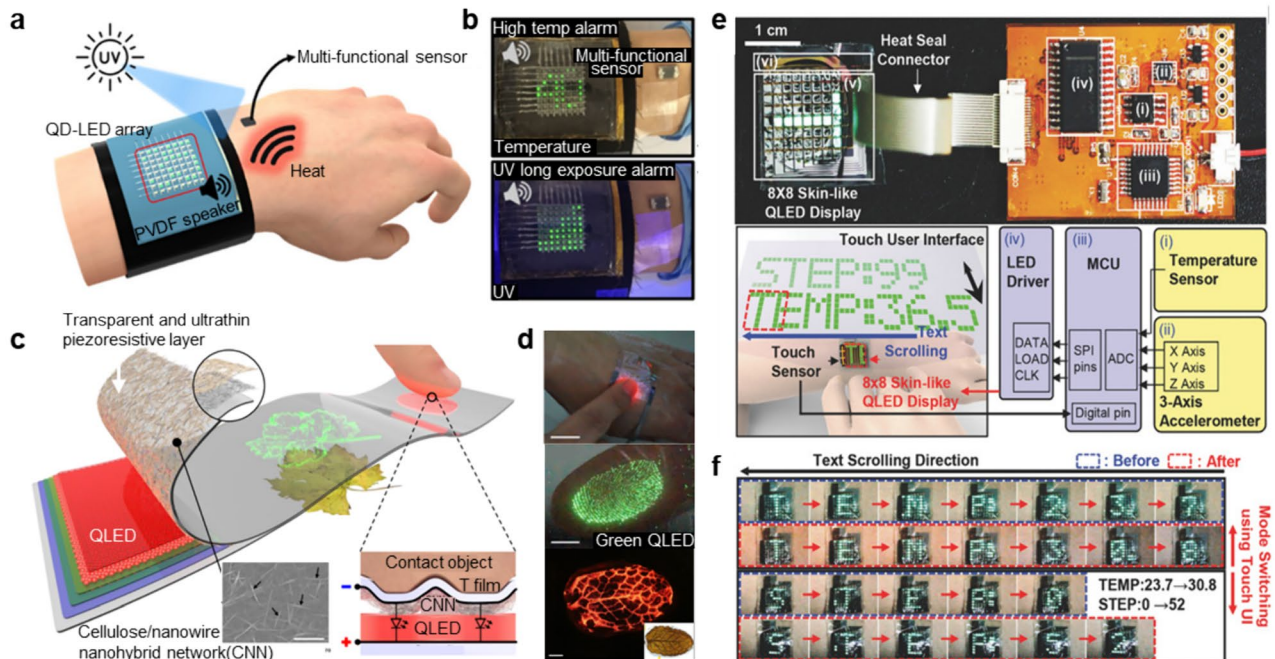### Light Sources for Wearable Healthcare System

Using LEDs instead of lasers as a light source in biomedical devices that are attached directly to the skin allows for the use of different wavelengths for broader applicability (Fig. 9g) [26]. For sensing, pulse oximetry utilizes LEDs to emit red and infrared light onto the skin. The photodetector then detects changes in light absorption after it passes through the blood and converts them into electrical signals [134]. Since oxygen level greatly affect the light absorption efficiency of hemoglobin, the blood oxygen levels (SpO$_2$) can be measured in real time by analyzing the absorption ratio. Photoplethysmogram (PPG) sensors also monitor changes in the bloodstream using a single wavelength, either green or red, in a non-invasive manner [135, 136]. Detection of the amount of light absorbed by the bloodstream provides information about cardiovascular conditions.

Phototherapeutic approaches generally use light to activate cells, channels, or implanted photosensitizers to initiate treatment mechanisms. In photodynamic therapy, LED light is irradiated to the pre-injected photosensitizers, which produce reactive oxygen species that kill cancer cells. Photobiomodulation facilitates the tissue regeneration by using light to modulate the production of chemicals involved in signal transduction. Furthermore, optogenetics uses light to stimulate to genetically modified light-gated ion channels, allowing for precise control of neural activities (Fig. 9h). Flexible QLEDs offer advantages for these applications because they conformally attach to the curved tissues, which can provide stable and accurate performance during dynamic activities.

Lee et al. reported a fiber-based quantum-dot pulse oximetry (FQPO) system consisting of flexible red/green QLEDs and organic photodetectors (Fig. 9i) [137]. The devices were fabricated using an ultrathin PET substrate for flexibility with a PEDOT:PSS transparent conductive electrode for light transmission. The FQPO-based PPG signal measurement was obtained from the left index finger and the

Applications of deformable QLEDs

I. Information displays integrated with sensors

II. Light sources for wearable healthcare
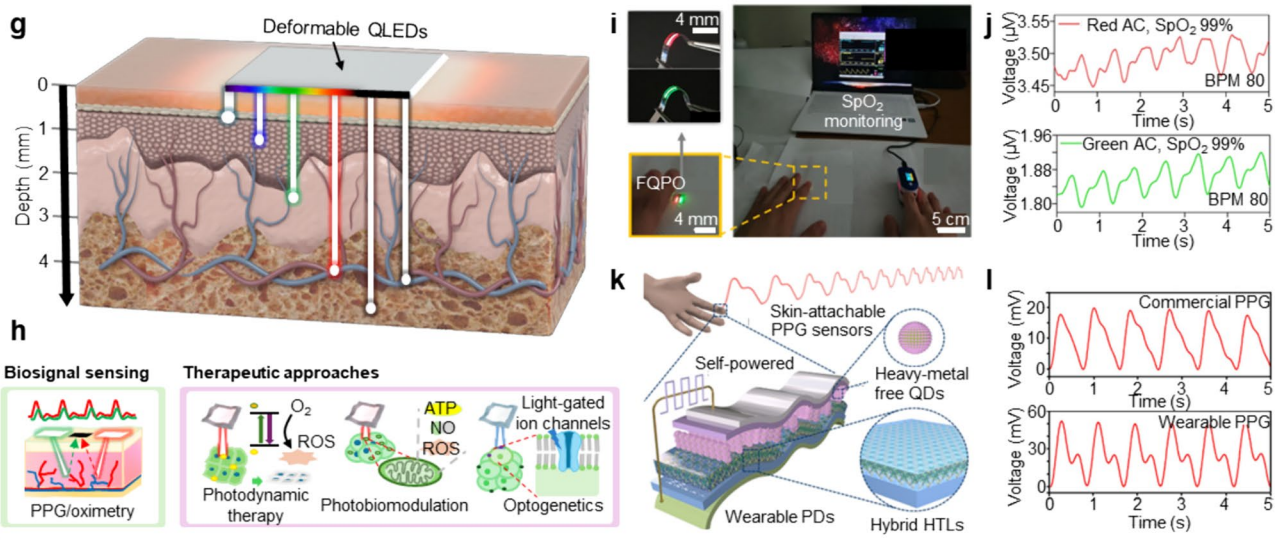
other PPG signal and SpO$_2$ data were obtained from the right index finger using commercially available pulse oximetry device. The FQPO collects stable PPG signal with direct current (DC) driving and performs accurate SpO$_2$ monitoring with alternating current (AC) driving (Fig. 9j). This system has long operational reliability, high wavelength selectivity (a narrow FWHM of 30 nm) with minimal influence from the waveguide mode noise signals. This study holds

potential for incorporating of pulse oximetry into wearable clothing.

QDs can be also applied for the light absorption layers in wearable photodetectors. Li et al. demonstrated a high performance wearable PPG sensor with wearable Cu-In-Se (CISe) QD photodetectors (QD-PDs) [138]. They proposed ultrathin self-powered QD-PDs using heavy-metal-free CISe QDs capped with iodide ions (I-) as ultrathin light

◀**Fig. 9** Applications of deformable QLEDs. **a** Schematic illustration of the skin-attached flexible QLED array and PVDF speaker with a multi-functional sensor. **b** Display of temperature (top) and UV exposure (bottom) by the QLED array. Audio signals is alerting noise that indicates high temperature or over-exposure to UV. Reproduced with permission from Ref. [132], Copyright 2022, American Chemical Society. **c** Schematic exploded illustration for device structure of an ultraflexible, transparent and pressure-sensitive photonic skin. The left inset shows SEM images of transparent electrode, while the right inset shows cross-sectional illustration of device under pressure. **d** Image of the photonic skin visualizing the pressure distribution in real-time. The top image shows the pressure imaging with the device laminated to the back of a hand. The middle image shows a device with a green QLED touched by a finger. The bottom image shows a pressure imaging using PDMS replica of a mint leaf. Scale bars, 5 mm. Reproduced with permission from Ref. [133], Copyright 2020, Springer Nature. **e** Image of the ultrathin QLED integrated with wearable electronics (top), and schematic illustration of the data flow between the integrated electronic components and QLED display (bottom). **f** Images of the skin-mounted QLED display visualizing the measured temperature and step count data in scroll mode. Reproduced with permission from Ref. [39], Copyright 2017, WILEY–VCH Verlag GmbH & Co. KGaA, Weinheim. **g** Schematic illustration of deformable QLEDs as light sources for wearable healthcare. **h** Schematic illustrations depicting the applications of deformable QLEDs in biosensing and therapeutic methods. Reproduced with permission from Ref. [26], Copyright 2024, Korean Journal of Chemical Engineering. **i** Images of the PPG signal measurement setup using FQPO for the left index finger and commercial pulse oximetry device for the right index finger. **j** SpO$_2$ monitoring with alternating current (AC) driving of the FQPO. Reproduced with permission from Ref. [137], Copyright 2023, Springer Nature. **k** Schematic illustration of ultrathin Cu-In-Se QD-PDs. **l** PPG signals measured by commercial rigid PD (top) and wearable PPG sensor with flexible CISe QD-PDs (bottom). Reproduced with permission from Ref. [138], Copyright 2023, American Chemical Society

absorption layers (~ 40 nm), which feature a high specific detectivity of 2.10×10^{12} Jones (Fig. 9k). A wearable PPG sensor consisting of commercial micro-LEDs and ultrathin CISe QD-PD was conformally applied around a fingertip, and PPG signal measurement was carried out in the photovoltage mode without external power supply. The wearable CISe-based PPG sensor detected the same heart rate (1.2 Hz) as that of the commercial rigid PPG sensor (Fig. 9l) regardless of the activity conditions of normal, exercise, and relaxation.

Conclusion

In this review, we provide an overview of the recent progress in deformable QLEDs, with a focus on material engineering and fabrication strategies. First, we provided an analysis of the developments for deformable QLED performance in terms of material and device engineering. We introduced various types of QDs and the operating principles of QLEDs, along with a summary of performance improvements in reported deformable devices. Three types of device

structures with regards to light-emission direction are introduced, and material candidates for soft substrates and transparent/semi-transparent electrodes are highlighted. Then, we examine unconventional fabrication strategies for deformable QLEDs. High-resolution patterning methods for QD thin films, which are crucial for the fabrication of full-color deformable QLEDs, are presented. Additionally, the article explored the latest studies on proof-of-concept deformable QLEDs with unusual form factors, including flexible, foldable, fiber-type, and stretchable QLEDs, detailing the materials and fabrication strategies for each form factor.

Despite significant advances in deformable QLEDs, several challenges remain that hinder their commercialization. A major issue is the insufficient stability of QLEDs based on heavy-metal-free QDs, especially for blue-emitting devices. Blue QDs, due to their small core size, have a higher proportion of surface defects that provide pathways for nonradiative exciton recombination. Additionally, a small offset between the conduction band minimum (CBM) of the core and the shell leads to inefficient charge confinement. Various theories have been proposed to explain the degradation of blue QLEDs, including QD oxidation followed by ligand detachment and HTL degradation due to excessive electron leakage. However, there is still an ongoing debate as to which of these is the primary cause. Currently, the best performance and stability for blue-emitting QDs are achieved with ZnTeSe/ZnSe/ZnS QDs, but QLEDs using these QDs still exhibit lower stability compared to commercial devices.

From a manufacturing perspective, reliable processes capable of producing high-resolution full-color devices should be developed. Inkjet printing is considered to be the most promising technology for industrial applications due to its cost-effectiveness and high throughput. For efficient printing of QD inks, high boiling point solvents, various stabilizers, and surfactants are generally required, and the composition of inks should be carefully designed to consider the wettability and elimination of coffee-ring effects. QD layers formed by inkjet printing differ significantly from those formed by spin coating using QD solutions dispersed in solvents such as octane, often resulting in lower electrical conductivity. Therefore, inks for HIL, HTL, and ETL materials should also be prepared to achieve high-performance fully inkjet-printed QLEDs.

The design strategies that grant deformability to QLEDs also face numerous challenges as well. For stretchable QLED arrays using island-bridge structures, additional technologies must be developed to compensate for the reduced image quality (*i.e.*, fill factor and resolution) during stretching. Intrinsically stretchable QLEDs are still in the early stages of development and require significant improvements in performance and stability. Moreover, ensuring a reliable stretchable encapsulation layer is critical. While thin film encapsulation using multilayer inorganic and organic structures

has been successful for commercial flexible OLEDs, such structures may not be suitable for stretchable encapsulants. Most organic elastomers have voids between the polymer chains, resulting in low barrier properties, necessitating the development of new barrier materials. We anticipate that advances in deformable QLEDs with high performance and longevity will drive significant potential in various applications, particularly next-generation free-form displays and optoelectronics for biomedical applications.

Declarations

Conflict of interests The authors declare no competing financial interests.

References

1. Z. Rao, F. Ershad, A. Almasri, L. Gonzalez, X. Wu, C. Yu, Adv. Mater. Technol. **5**, 2000233 (2020)
2. C. Wang, C. Wang, Z. Huang, S. Xu, Adv. Mater. **30**, 1801368 (2018)
3. D.C. Kim, H.J. Shim, W. Lee, J.H. Koo, D.H. Kim, Adv. Mater. **32**, 1902743 (2020)
4. J.C. Yang, J. Mun, S.Y. Kwon, S. Park, Z. Bao, S. Park, Adv. Mater. **31**, 1904765 (2019)
5. S. Wang, J.Y. Oh, J. Xu, H. Tran, Z. Bao, Accounts Chem. Res. **51**, 1033 (2018)
6. K. Kim, M. Kim, J. Yang, Korean J. Chem. Eng. (2024). https://doi.org/10.1007/s11814-024-00179-1
7. S.-H. Sunwoo, S.I. Han, C.S. Park, J.H. Kim, J.S. Georgiou, S.-P. Lee, D.-H. Kim, T. Hyeon, Nat. Rev. Bioeng. **2**, 8 (2024)
8. M. Kim, H. Lee, S. Nam, D.-H. Kim, G.D. Cha, Accounts Chem. Res. **57**, 1633 (2024)
9. X. Wang, Z. Liu, T. Zhang, Small **13**, 1602790 (2017)
10. Y. Liu, M. Pharr, G.A. Salvatore, ACS Nano **11**, 9614 (2017)
11. D.C. Kim, H. Yun, J. Kim, H. Seung, W.S. Yu, J.H. Koo, J. Yang, J.H. Kim, T. Hyeon, D.-H. Kim, Nat. Electron. **4**, 671 (2021)
12. Y. Luo, M.R. Abidian, J.H. Ahn, D. Akinwande, A.M. Andrews, M. Antonietti, Z. Bao, M. Berggren, C.A. Berkey, C.J. Bettinger, J. Chen, P. Chen, W. Cheng, X. Cheng, S.J. Choi, A. Chortos, C. Dagdeviren, R.H. Dauskardt, C.A. Di, M.D. Dickey, X. Duan, A. Facchetti, Z. Fan, Y. Fang, J. Feng, X. Feng, H. Gao, W. Gao, X. Gong, C.F. Guo, X. Guo, M.C. Hartel, Z. He, J.S. Ho, Y. Hu, Q. Huang, Y. Huang, F. Huo, M.M. Hussain, A. Javey, U. Jeong, C. Jiang, X. Jiang, J. Kang, D. Karnaushenko, A. Khademhosseini, D.H. Kim, I.D. Kim, D. Kireev, L. Kong, C. Lee, N.E. Lee, P.S. Lee, T.W. Lee, F. Li, J. Li, C. Liang, C.T. Lim, Y. Lin, D.J. Lipomi, J. Liu, K. Liu, N. Liu, R. Liu, Y. Liu, Y. Liu, Z. Liu, Z. Liu, X.J. Loh, N. Lu, Z. Lv, S. Magdassi, G.G. Malliaras, N. Matsuhisa, A. Nathan, S. Niu, J. Pan, C. Pang, Q. Pei, H. Peng, D. Qi, H. Ren, J.A. Rogers, A. Rowe, O.G. Schmidt, T. Sekitani, D.G. Seo, G. Shen, X. Sheng, Q. Shi, T. Someya, Y. Song, E. Stavrinidou, M. Su, X. Sun, K. Takei, X.M. Tao, B.C.K. Tee, A.V. Thean, T.Q. Trung, C. Wan, H. Wang, J. Wang, M. Wang, S. Wang, T. Wang, Z.L. Wang, P.S. Weiss, H. Wen, S. Xu, T. Xu, H. Yan, X. Yan, H. Yang, L. Yang, S. Yang, L. Yin, C. Yu, G. Yu, J. Yu, S.H. Yu, X. Yu, E. Zamburg, H. Zhang, X. Zhang, X. Zhang, X. Zhang, Y. Zhang, Y. Zhang, S. Zhao, X. Zhao, Y. Zheng, Y.Q. Zheng, Z. Zheng, T. Zhou, B. Zhu, M. Zhu, R. Zhu, Y. Zhu, Y. Zhu, G. Zou, X. Chen, ACS Nano **17**, 5211 (2023)
13. J.-K. Song, J. Kim, J. Yoon, J.H. Koo, H. Jung, K. Kang, S.-H. Sunwoo, S. Yoo, H. Chang, J. Jo, W. Baek, S. Lee, M. Lee, H. Kim, M. Shin, Y. Yoo, Y. Song, T. Hyeon, D.-H. Kim, D.H. Son, Nat. Nanotechnol. **17**, 849 (2022)
14. J. Wang, M. Sotzing, M. Lee, A. Chortos, Sci. Adv. **9**, eadg8019 (2023)
15. J. Ko, C. Kim, D. Kim, Y. Song, S. Lee, B. Yeom, J. Huh, S. Han, D. Kang, J.-S. Koh, Sci. Robot. **7**, 6463 (2022)
16. D. Zhong, C. Wu, Y. Jiang, Y. Yuan, M.G. Kim, Y. Nishio, C.C. Shih, W. Wang, J.C. Lai, X. Ji, T.Z. Gao, Y.X. Wang, C. Xu, Y. Zheng, Z. Yu, H. Gong, N. Matsuhisa, C. Zhao, Y. Lei, D. Liu, S. Zhang, Y. Ochiai, S. Liu, S. Wei, J.B. Tok, Z. Bao, Nature **627**, 313 (2024)
17. J.H. Koo, J. Kang, S. Lee, J.-K. Song, J. Choi, J. Yoon, H.J. Park, S.-H. Sunwoo, D.C. Kim, W. Nam, D.-H. Kim, S.G. Im, D.H. Son, Nat. Electron. **6**, 137 (2023)
18. X. Chen, C. S. Hwang, Y. van de Burgt, F. Santoro, Mater. Horizons (2024). https://doi.org/10.1039/d4mh90052a
19. T.U. Nam, N.T.P. Vo, M.W. Jeong, K.H. Jung, S.H. Lee, T.I. Lee, J.Y. Oh, ACS Nano **18**, 14558 (2024)
20. J. Pu, Q. Cao, Y. Gao, Q. Wang, Z. Geng, L. Cao, F. Bu, N. Yang, C. Guan, Adv. Mater. **36**, 2305812 (2024)
21. S.H. Kim, A. Basir, R. Avila, J. Lim, S.W. Hong, G. Choe, J.H. Shin, J.H. Hwang, S.Y. Park, J. Joo, C. Lee, J. Choi, B. Lee, K.-S. Choi, S. Jung, T.-I. Kim, H. Yoo, Y.H. Jung, Nature **629**, 1047 (2024)
22. S. Chang, J.H. Koo, J. Yoo, M.S. Kim, M.K. Choi, D.-H. Kim, Y.M. Song, Chem. Rev. **124**, 768 (2024)
23. Z. Zhang, Y. Wang, S. Jia, C. Fan, Nat. Photonics **18**, 114 (2024)
24. D.W. Kim, S.W. Kim, G. Lee, J. Yoon, S. Kim, J.-H. Hong, S.-C. Jo, U. Jeong, Light Sci. Appl. **12**, 61 (2023)
25. J.H. Koo, D.C. Kim, H.J. Shim, T.H. Kim, D.H. Kim, Adv. Funct. Mater. **28**, 1801834 (2018)
26. G.D. Cha, D.-H. Kim, D.C. Kim, Korean J. Chem. Eng. **41**, 1 (2024)
27. J.-K. Song, M.S. Kim, S. Yoo, J.H. Koo, D.-H. Kim, Nano Res. **14**, 2919 (2021)
28. Y.F. Liu, J. Feng, Y.G. Bi, D. Yin, H.B. Sun, Adv. Mater. Technol. **4**, 1800371 (2019)
29. J. Yang, M.K. Choi, U.J. Yang, S.Y. Kim, Y.S. Kim, J.H. Kim, D.-H. Kim, T. Hyeon, Nano Lett. **21**, 26 (2020)
30. M.K. Choi, J. Yang, T. Hyeon, D.-H. Kim, npj Flex Electron. **2**, 10 (2018)
31. J.H. Jang, S. Li, D.H. Kim, J. Yang, M.K. Choi, Adv. Electron. Mater. **9**, 2201271 (2023)
32. Q. Lin, Y. Zhu, Y. Wang, D. Li, Y. Zhao, Y. Liu, F. Li, W. Huang, Adv. Mater. **35**, 2210385 (2023)
33. D. Tian, H. Ma, G. Huang, M. Gao, F. Cai, Y. Fang, C. Li, X. Jiang, A. Wang, S. Wang, Z. Du, Adv. Opt. Mater. **11**, 2201965 (2023)
34. J. Kim, J. Roh, M. Park, C. Lee, Adv. Mater. **36**, 2212220 (2023)
35. E. Jang, H. Jang, Chem. Rev. **123**, 4663 (2023)
36. T.-H. Kim, K.-S. Cho, E.K. Lee, S.J. Lee, J. Chae, J.W. Kim, D.H. Kim, J.-Y. Kwon, G. Amaratunga, S.Y. Lee, B.L. Choi, Y. Kuk, J.M. Kim, K. Kim, Nat. Photonics **5**, 176 (2011)
37. X. Yang, E. Mutlugun, C. Dang, K. Dev, Y. Gao, S.T. Tan, X.W. Sun, H.V. Demir, ACS Nano **8**, 8224 (2014)
38. M.K. Choi, J. Yang, K. Kang, D.C. Kim, C. Choi, C. Park, S.J. Kim, S.I. Chae, T.-H. Kim, J.H. Kim, T. Hyeon, D.-H. Kim, Nat. Commun. **6**, 7149 (2015)
39. J. Kim, H.J. Shim, J. Yang, M.K. Choi, D.C. Kim, J. Kim, T. Hyeon, D.H. Kim, Adv. Mater. **29**, 1700217 (2017)

40. M.K. Choi, J. Yang, D.C. Kim, Z. Dai, J. Kim, H. Seung, V.S. Kale, S.J. Sung, C.R. Park, N. Lu, T. Hyeon, D.-H. Kim, Adv. Mater. **30**, 1703279 (2018)

41. S. Lee, H.W. Choi, C.L. Figueiredo, D.-W. Shin, F.M. Moncunill, K. Ullrich, S. Sinopoli, P. Jovančić, J. Yang, H. Lee, M. Eisenreich, U. Emanuele, S. Nicotera, A. Santos, R. Igreja, A. Marrani, R. Momentè, J. Gomes, S.-M. Jung, S.D. Han, S.Y. Bang, S. Zhan, W. Harden-Chaters, Y.H. Suh, X.-B. Fan, T.H. Lee, J.-W. Jo, Y. Kim, A. Costantino, V.G. Candel, N. Durães, S. Meyer, C.-H. Kim, M. Lucassen, A. Nejim, D. Jiménez, M. Springer, Y.-W. Lee, G.-H. An, Y. Choi, J.I. Sohn, S. Cha, M. Chhowalla, G.A.J. Amaratunga, L.G. Occhipinti, P. Barquinha, E. Fortunato, R. Martins, J.M. Kim, Sci. Adv. **9**, eadf4049 (2023)

42. D.C. Kim, H. Seung, J. Yoo, J. Kim, H.H. Song, J.S. Kim, Y. Kim, K. Lee, C. Choi, D. Jung, C. Park, H. Heo, J. Yang, T. Hyeon, M.K. Choi, D.-H. Kim, Nat. Electron. **7**, 365 (2024)

43. V.L. Colvin, M.C. Schlamp, A.P. Alivisatos, Nature **370**, 354 (1994)

44. J. Yang, M.K. Choi, D.H. Kim, T. Hyeon, Adv. Mater. **28**, 1176 (2016)

45. P.O. Anikeeva, J.E. Halpert, M.G. Bawendi, V. Bulovic, Nano Lett. **9**, 2532 (2009)

46. H. Xu, J. Song, P. Zhou, Y. Song, J. Xu, H. Shen, S. Fang, Y. Gao, Z. Zuo, J.M. Pina, O. Voznyy, C. Yang, Y. Hu, J. Li, J. Du, E.H. Sargent, F. Fan, Nat. Photonics **18**, 186 (2024)

47. Y.-H. Won, O. Cho, T. Kim, D.-Y. Chung, T. Kim, H. Chung, H. Jang, J. Lee, D. Kim, E. Jang, Nature **575**, 634 (2019)

48. T. Kim, K.-H. Kim, S. Kim, S.-M. Choi, H. Jang, H.-K. Seo, H. Lee, D.-Y. Chung, E. Jang, Nature **586**, 385 (2020)

49. W. Song, K.C. Chong, G. Qi, Y. Xiao, G. Chen, B. Li, Y. Tang, X. Zhang, Y. Yao, Z. Lin, Z. Zou, B. Liu, J. Am. Chem. Soc. **146**, 3303 (2024)

50. G.C. Adhikari, P.A. Vargas, H. Zhu, A. Grigoriev, P. Zhu, Nanoscale Adv. **1**, 1791 (2019)

51. L. Protesescu, S. Yakunin, M.I. Bodnarchuk, F. Krieg, R. Caputo, C.H. Hendon, R.X. Yang, A. Walsh, M.V. Kovalenko, Nano Lett. **15**, 3692 (2015)

52. Y. Dong, T. Qiao, D. Kim, D. Parobek, D. Rossi, D.H. Son, Nano Lett. **18**, 3716 (2018)

53. N. Wang, L. Cheng, R. Ge, S. Zhang, Y. Miao, W. Zou, C. Yi, Y. Sun, Y. Cao, R. Yang, Y. Wei, Q. Guo, Y. Ke, M. Yu, Y. Jin, Y. Liu, Q. Ding, D. Di, L. Yang, G. Xing, H. Tian, C. Jin, F. Gao, R.H. Friend, J. Wang, W. Huang, Nat. Photonics **10**, 699 (2016)

54. J.S. Kim, J.-M. Heo, G.-S. Park, S.-J. Woo, C. Cho, H.J. Yun, D.-H. Kim, J. Park, S.-C. Lee, S.-H. Park, E. Yoon, N.C. Greenham, T.-W. Lee, Nature **611**, 688 (2022)

55. B.S. Mashford, M. Stevenson, Z. Popovic, C. Hamilton, Z. Zhou, C. Breen, J. Steckel, V. Bulovic, M. Bawendi, S. Coe-Sullivan, P.T. Kazlas, Nat. Photonics **7**, 407 (2013)

56. J. Kwak, W.K. Bae, D. Lee, I. Park, J. Lim, M. Park, H. Cho, H. Woo, D.Y. Yoon, K. Char, S. Lee, C. Lee, Nano Lett. **12**, 2362 (2012)

57. Y. Zou, Y. Liu, M. Ban, Q. Huang, T. Sun, Q. Zhang, T. Song, B. Sun, Nanoscale Horiz. **2**, 156 (2017)

58. A. Wang, H. Shen, S. Zang, Q. Lin, H. Wang, L. Qian, J. Niu, L.S. Li, Nanoscale **7**, 2951 (2015)

59. X. Zhang, H. Dai, J. Zhao, S. Wang, X. Sun, Thin Solid Films **603**, 187 (2016)

60. M.D. Ho, D. Kim, N. Kim, S.M. Cho, H. Chae, A.C.S. Appl. Mater. Interfaces **5**, 12369 (2013)

61. T. Davidson-Hall, H. Aziz, A.C.S. Appl, Mater. Interfaces **12**, 16782 (2020)

62. J. Lim, M. Park, W.K. Bae, D. Lee, S. Lee, C. Lee, K. Char, ACS Nano **7**, 9019 (2013)

63. W. Ji, Y. Tian, Q. Zeng, S. Qu, L. Zhang, P. Jing, J. Wang, J. Zhao, A.C.S. Appl, Mater. Interfaces **6**, 14001 (2014)

64. S. Rhee, J.H. Chang, D. Hahm, B.G. Jeong, J. Kim, H. Lee, J. Lim, E. Hwang, J. Kwak, W.K. Bae, ACS Nano **14**, 17496 (2020)

65. H. Yu, H. Zhu, M. Xu, J. Zhang, H. Feng, L. Zhang, S. Liu, W. Xie, ACS Photonics **10**, 2192 (2022)

66. F. Qin, T. Li, M. Lu, S. Sun, P. Lu, X. Li, N. Feng, Y. Zhang, Y. Gao, Z. Wu, J. Hu, F. Yan, X. Bai, A.C.S. Appl, Mater. Interfaces **15**, 47278 (2023)

67. W.C. Choy, J. Niu, W. Li, P. Chui, J. Phys. D Appl. Phys. **41**, 025106 (2007)

68. G. Liu, X. Zhou, S. Chen, A.C.S. Appl, Mater. Interfaces **8**, 16768 (2016)

69. R. Yu, F. Yin, X. Huang, W. Ji, J. Mater. Chem. C **5**, 6682 (2017)

70. J.I. Kwon, G. Park, G.H. Lee, J.H. Jang, N.J. Sung, S.Y. Kim, J. Yoo, K. Lee, H. Ma, M. Karl, T.J. Shin, M.H. Song, J. Yang, M.K. Choi, Sci. Adv. **8**, eadd0697 (2022)

71. S. Hong, H. Lee, J. Lee, J. Kwon, S. Han, Y.D. Suh, H. Cho, J. Shin, J. Yeo, S.H. Ko, Adv. Mater. (Deerfield Beach Fla.) **27**, 4744 (2015)

72. F. Xu, Y. Zhu, Adv. Mater. **24**, 5117 (2012)

73. A.R. Madaria, A. Kumar, C. Zhou, Nanotechnology **22**, 245201 (2011)

74. S. Bae, H. Kim, Y. Lee, X. Xu, J.S. Park, Y. Zheng, J. Balakrishnan, T. Lei, H.R. Kim, Y.I. Song, Y.J. Kim, K.S. Kim, B. Özyilmaz, J.H. Ahn, B.H. Hong, S. Iijima, Nat. Nanotechnol. **5**, 574 (2010)

75. K.S. Kim, Y. Zhao, H. Jang, S.Y. Lee, J.M. Kim, K.S. Kim, J.-H. Ahn, P. Kim, J.-Y. Choi, B.H. Hong, Nature **457**, 706 (2009)

76. U. Kim, J. Kang, C. Lee, H.Y. Kwon, S. Hwang, H. Moon, J.C. Koo, J.-D. Nam, B.H. Hong, J.-B. Choi, Nanotechnology **24**, 145501 (2013)

77. X. Huang, Z. Zeng, Z. Fan, J. Liu, H. Zhang, Adv. Mater. **24**, 5979 (2012)

78. W. Jiang, S. Lee, K. Zhao, K. Lee, H. Han, J. Oh, H. Lee, H. Kim, C.M. Koo, C.M. Park, ACS Nano **16**, 9203 (2022)

79. S. Ahn, T.H. Han, K. Maleski, J. Song, Y.H. Kim, M.H. Park, H. Zhou, S. Yoo, Y. Gogotsi, T.W. Lee, Adv. Mater. **32**, 2000919 (2020)

80. H. Zhou, S.J. Han, H.D. Lee, D. Zhang, M. Anayee, S.H. Jo, Y. Gogotsi, T.W. Lee, Adv. Mater. **34**, 2206377 (2022)

81. M.K. Choi, I. Park, D.C. Kim, E. Joh, O.K. Park, J. Kim, M. Kim, C. Choi, J. Yang, K.W. Cho, J.-H. Hwang, J.-M. Nam, T. Hyeon, J.H. Kim, D.-H. Kim, Adv. Funct. Mater. **25**, 7109 (2015)

82. C. Dang, J. Lee, C. Breen, J.S. Steckel, S. Coe-Sullivan, A. Nurmikko, Nat. Nanotechnol. **7**, 335 (2012)

83. J.K. Song, D. Son, J. Kim, Y.J. Yoo, G.J. Lee, L. Wang, M.K. Choi, J. Yang, M. Lee, K. Do, J.H. Koo, N. Lu, J.H. Kim, T. Hyeon, Y.M. Song, D.-H. Kim, Adv. Funct. Mater. **27**, 1605286 (2017)

84. J. Park, H. Seung, D.C. Kim, M.S. Kim, D.H. Kim, Adv. Funct. Mater. **31**, 2009281 (2021)

85. C. Luo, Z. Zheng, Y. Ding, Z. Ren, H. Shi, H. Ji, X. Zhou, Y. Chen, Adv. Mater. **35**, 2303329 (2023)

86. K. Yin, E.-L. Hsiang, J. Zou, Y. Li, Z. Yang, Q. Yang, P.-C. Lai, C.-L. Lin, S.-T. Wu, Light Sci. Appl. **11**, 161 (2022)

87. T. Yokota, P. Zalar, M. Kaltenbrunner, H. Jinno, N. Matsuhisa, H. Kitanosako, Y. Tachibana, W. Yukita, M. Koizumi, T. Someya, Sci. Adv. **2**, e1501856 (2016)

88. T.H. Kim, D.Y. Chung, J. Ku, I. Song, S. Sul, D.H. Kim, K.S. Cho, B.L. Choi, J.M. Kim, S. Hwang, K. Kim, Nat. Commun. **4**, 2637 (2013)

89. M.A. Meitl, Z.-T. Zhu, V. Kumar, K.J. Lee, X. Feng, Y.Y. Huang, I. Adesida, R.G. Nuzzo, J.A. Rogers, Nat. Mater. **5**, 33 (2006)

90. C. Linghu, S. Zhang, C. Wang, J. Song, npj Flex Electron. **2**, 26 (2018)

91. A. Carlson, A.M. Bowen, Y. Huang, R.G. Nuzzo, J.A. Rogers, Adv. Mater. **24**, 5284 (2012)

92. B. Derby, Ann. Rev. Mater. Res. **40**, 395 (2010)
93. B.J. De Gans, P.C. Duineveld, U.S. Schubert, Adv. Mater. **16**, 203 (2004)
94. P. Yang, L. Zhang, D.J. Kang, R. Strahl, T. Kraus, Adv. Opt. Mater. **8**, 1901429 (2020)
95. P.J. Yunker, T. Still, M.A. Lohr, A. Yodh, Nature **476**, 308 (2011)
96. M.S. Onses, E. Sutanto, P.M. Ferreira, A.G. Alleyne, J.A. Rogers, Small **11**, 4237 (2015)
97. J.-U. Park, M. Hardy, S.J. Kang, K. Barton, K. Adair, D.K. Mukhopadhyay, C.Y. Lee, M.S. Strano, A.G. Alleyne, J.G. Georgiadis, P.M. Ferreira, J.A. Rogers, Nat. Mater. **6**, 782 (2007)
98. H. Wang, Y. Zhang, Y. Liu, Z. Chen, Y. Li, X. Li, X. Xu, Nanoscale Adv. **5**, 1183 (2023)
99. L. Li, X. Liu, S. Pal, S. Wang, C.K. Ober, E.P. Giannelis, Chem. Soc. Rev. **46**, 4855 (2017)
100. S. Myeong, B. Chon, S. Kumar, H.-J. Son, S.O. Kang, S. Seo, Nanoscale Adv. **4**, 1080 (2022)
101. G.-H. Kim, J. Lee, J.Y. Lee, J. Han, Y. Choi, C.J. Kang, K.-B. Kim, W. Lee, J. Lim, S.-Y. Cho, A.C.S. Appl, Mater. Interfaces **13**, 43075 (2021)
102. W. Mei, Z. Zhang, A. Zhang, D. Li, X. Zhang, H. Wang, Z. Chen, Y. Li, X. Li, X. Xu, Nano Res. **13**, 2485 (2020)
103. J. Yang, D. Hahm, K. Kim, S. Rhee, M. Lee, S. Kim, J.H. Chang, H.W. Park, J. Lim, M. Lee, H. Kim, J. Bang, H. Ahn, J.H. Cho, J. Kwak, B. Kim, C. Lee, W.K. Bae, M.S. Kang, Nat. Commun. **11**, 2874 (2020)
104. D. Hahm, J. Lim, H. Kim, J.-W. Shin, S. Hwang, S. Rhee, J.H. Chang, J. Yang, C.H. Lim, H. Jo, B. Choi, N.S. Cho, Y.-S. Park, D.C. Lee, E. Hwang, S. Chung, C.-M. Kang, M.S. Kang, W.K. Bae, Nat. Nanotechnol. **17**, 952 (2022)
105. X. Dai, Z. Zhang, Y. Jin, Y. Niu, H. Cao, X. Liang, L. Chen, J. Wang, X. Peng, Nature **515**, 96 (2014)
106. H. Shen, Q. Gao, Y. Zhang, Y. Lin, Q. Lin, Z. Li, L. Chen, Z. Zeng, X. Li, Y. Jia, S. Wang, Z. Du, L.S. Li, Z. Zhang, Nat. Photonics **13**, 192 (2019)
107. D. Jung, C. Lim, H.J. Shim, Y. Kim, C. Park, J. Jung, S.I. Han, S.H. Sunwoo, K.W. Cho, G.D. Cha, D.C. Kim, J.H. Koo, J.H. Kim, T. Hyeon, D.H. Kim, Science **373**, 1022 (2021)
108. S.-H. Sunwoo, K.-H. Ha, S. Lee, N. Lu, D.-H. Kim, Annu. Rev. Chem. Biomol. Engineer. **12**, 359 (2021)
109. B. O'Connor, K.H. An, Y. Zhao, K.P. Pipe, M. Shtein, Adv. Mater. **19**, 3897 (2007)
110. Q. Shan, C. Wei, Y. Jiang, J. Song, Y. Zou, L. Xu, T. Fang, T. Wang, Y. Dong, J. Liu, B. Han, F. Zhang, J. Chen, Y. Wang, H. Zeng, Light Sci. Appl. **9**, 163 (2020)
111. A. Leal-Junior, L. Avellar, A. Frizera, C. Marques, Sci. Rep. **10**, 13867 (2020)
112. C.J. Brinker, G. Frye, A. Hurd, C. Ashley, Thin Solid Films **201**, 97 (1991)
113. L. Pawlowski, Surf. Coat. Technol. **203**, 2807 (2009)
114. K. Kim, Y.G. Park, B.G. Hyun, M. Choi, J.U. Park, Adv. Mater. **31**, 1804690 (2019)
115. J. Yoo, S. Li, D.-H. Kim, J. Yang, M.K. Choi, Nanoscale Horiz. **7**, 801 (2022)
116. D.S. Ginley, C. Bright, MRS Bull. **25**, 15 (2000)
117. T.-H. Han, Y. Lee, M.-R. Choi, S.-H. Woo, S.-H. Bae, B.H. Hong, J.-H. Ahn, T.-W. Lee, Nat. Photonics **6**, 105 (2012)
118. D. Yin, J. Feng, R. Ma, Y.-F. Liu, Y.-L. Zhang, X.-L. Zhang, Y.-G. Bi, Q.-D. Chen, H.-B. Sun, Nat. Commun. **7**, 11573 (2016)
119. Y. Yang, Y. Zheng, W. Cao, A. Titov, J. Hyvonen, J.R. Manders, J. Xue, P.H. Holloway, L. Qian, Nat. Photonics **9**, 259 (2015)
120. H. Cho, S.-H. Jeong, M.-H. Park, Y.-H. Kim, C. Wolf, C.-L. Lee, J.H. Heo, A. Sadhanala, N. Myoung, S. Yoo, S.H. Im, R.H. Friend, T.-W. Lee, Science **350**, 1222 (2015)
121. M. Yuan, L.N. Quan, R. Comin, G. Walters, R. Sabatini, O. Voznyy, S. Hoogland, Y. Zhao, E.M. Beauregard, P.

122. Y. Lee, D.S. Kim, S.W. Jin, H. Lee, Y.R. Jeong, I. You, G. Zi, J.S. Ha, Chem. Eng. J. **427**, 130858 (2022)
123. S.H. Kim, G.W. Baek, J. Yoon, S. Seo, J. Park, D. Hahm, J.H. Chang, D. Seong, H. Seo, S. Oh, K. Kim, H. Jung, Y. Oh, H.W. Baac, B. Alimkhanuly, W.K. Bae, S. Lee, M. Lee, J. Kwak, J.-H. Park, D. Son, Adv. Mater. **33**, 2104690 (2021)
124. Y.F. Li, S.Y. Chou, P. Huang, C. Xiao, X. Liu, Y. Xie, F. Zhao, Y. Huang, J. Feng, H. Zhong, H.-B. Sun, Q. Pei, Adv. Mater. **31**, 1807516 (2019)
125. T.-H. Kim, C.-S. Lee, S. Kim, J. Hur, S. Lee, K.W. Shin, Y.-Z. Yoon, M.K. Choi, J. Yang, D.-H. Kim, T. Hyeon, S. Park, S. Hwang, ACS Nano **11**, 5992 (2017)
126. N. Matsuhisa, S. Niu, S.J. O'Neill, J. Kang, Y. Ochiai, T. Katsumata, H.-C. Wu, M. Ashizawa, G.-J.N. Wang, D. Zhong, X. Wang, X. Gong, R. Ning, H. Gong, I. You, Y. Zheng, Z. Zhang, J.B.-H. Tok, X. Chen, Z. Bao, Nature **600**, 246 (2021)
127. M.W. Jeong, J.H. Ma, J.S. Shin, J.S. Kim, G. Ma, T.U. Nam, X. Gu, S.J. Kang, J.Y. Oh, Sci. Adv. **9**, eadh1504 (2023)
128. Z. Zhang, W. Wang, Y. Jiang, Y.-X. Wang, Y. Wu, J.-C. Lai, S. Niu, C. Xu, C.-C. Shih, C. Wang, H. Yan, L. Galuska, N. Prine, H.-C. Wu, D. Zhong, G. Chen, N. Matsuhisa, Y. Zheng, Z. Yu, Y. Wang, R. Dauskardt, X. Gu, J.B.-H. Tok, Z. Bao, Nature **603**, 624 (2022)
129. J.H. Koo, H. Yun, W. Lee, S.-H. Sunwoo, H.J. Shim, D.-H. Kim, Opto-Electron. Adv. **5**, 210131 (2022)
130. M.A. Triana, E.-L. Hsiang, C. Zhang, Y. Dong, S.-T. Wu, ACS Energy Lett. **7**, 1001 (2022)
131. J. Kim, J. Lee, D. Son, M.K. Choi, D.-H. Kim, Nano Converg. **3**, 1 (2016)
132. Y. Lee, G. Jung, S.W. Jin, J.S. Ha, A.C.S. Appl, Mater. Interfaces **14**, 48844 (2022)
133. B. Lee, J.-Y. Oh, H. Cho, C.W. Joo, H. Yoon, S. Jeong, E. Oh, J. Byun, H. Kim, S. Lee, J. Seo, C.W. Park, S. Choi, N.-M. Park, S.-Y. Kang, C.-S. Hwang, S.-D. Ahn, J.-I. Lee, Y. Hong, Nat. Commun. **11**, 663 (2020)
134. H. Seung, C. Choi, D.C. Kim, J.S. Kim, J.H. Kim, J. Kim, S.I. Park, J.A. Lim, J. Yang, M.K. Choi, T. Hyeon, D.-H. Kim, Sci. Adv. **8**, eabq3101 (2022)
135. T. Chen, Z. Liu, L. Zhang, H. Wu, G. Wu, H. Chen, A.C.S. Appl, Mater. Interfaces **15**, 50312 (2023)
136. J. Mathew, D. Zheng, J. Xu, H. Liu, Adv. Electron. Mater. (2024). https://doi.org/10.1002/aelm.202300765
137. H.S. Lee, B. Noh, S.U. Kong, Y.H. Hwang, H.-E. Cho, Y. Jeon, K.C. Choi, npj Flex Electron. **7**, 15 (2023)
138. S. Li, J.H. Jang, W. Chung, H. Seung, S.I. Park, H. Ma, W.J. Pyo, C. Choi, D.S. Chung, D.-H. Kim, ACS Nano **17**, 20013 (2023)
139. Y. Kim, T. Greco, C. Ippen, A. Wedel, J. Kim, IEEE, 425–427 (2013).
140. Y. Fang, K. Ding, Z. Wu, H. Chen, W. Li, S. Zhao, Y. Zhang, L. Wang, J. Zhou, B. Hu, ACS Nano **10**, 10023 (2016)
141. D. Kim, Y. Fu, S. Kim, W. Lee, K.-H. Lee, H.K. Chung, H.-J. Lee, H. Yang, H. Chae, ACS Nano **11**, 1982 (2017)
142. F. Zhao, D. Chen, S. Chang, H. Huang, K. Tong, C. Xiao, S. Chou, H. Zhong, Q. Pei, J. Mater. Chem. C **5**, 531 (2017)
143. Y. Sun, W. Chen, Y. Wu, Z. He, S. Zhang, S. Chen, Nanoscale **11**, 1021 (2019)
144. K. Ding, Y. Fang, S. Dong, H. Chen, B. Luo, K. Jiang, H. Gu, L. Fan, S. Liu, B. Hu, L. Wang, Adv. Opt. Mater. **6**, 1800347 (2018)
145. P. Shen, X. Li, F. Cao, X. Ding, X. Yang, J. Mater. Chem. C **6**, 9642 (2018)
146. H. Chen, T.H. Yeh, J. He, C. Zhang, R. Abbel, M.R. Hamblin, Y. Huang, R.J. Lanzafame, I. Stadler, J. Celli, S.-W. Liu, S.-T. Wu, Y. Dong, J. Soc. Inf. Disp. **26**, 296 (2018)

Kanjanaboos, Z. Lu, D.H. Kim, E.H. Sargent, Nat. Nanotechnol. **11**, 872 (2016)

147. L. Xue, Y. Liu, F. Li, K. Sun, W. Chen, K. Yang, H. Hu, J. Lin, H. Chen, Z. Yang, T. Guo, Vacuum **163**, 282 (2019)
148. D. Hahm, J.H. Chang, B.G. Jeong, P. Park, J. Kim, S. Lee, J. Choi, W.D. Kim, S. Rhee, J. Lim, D.C. Lee, C. Lee, K. Char, W.K. Bae, Chem. Mat. **31**, 3476 (2019)
149. D.W. Shin, Y.H. Suh, S. Lee, B. Hou, S.D. Han, Y. Cho, X.B. Fan, S.Y. Bang, S. Zhan, J. Yang, H.W. Choi, S. Jung, F.C. Mocanu, H. Lee, L. Occhipinti, Y.T. Chun, G. Amaratunga, J.M. Kim, Adv. Opt. Mater. **8**, 1901 (2020)
150. D.-H. Jiang, Y.-C. Liao, C.-J. Cho, L. Veeramuthu, F.-C. Liang, T.-C. Wang, C.-C. Chueh, T. Satoh, S.-H. Tung, C.-C. Kuo, A.C.S. Appl, Mater. Interfaces **12**, 14408 (2020)
151. R. Wang, T. Wang, Z. Kang, H. Zhang, R. Yu, W. Ji, Opt. Express **30**, 15747 (2022)
152. H.-Y. Liu, W.-Y. Su, C.-J. Chang, S.-Y. Lin, C.-Y. Huang, A.C.S. Appl, Mater. Interfaces **14**, 36855 (2022)
153. C. Chen, T. Xuan, Y. Yang, F. Huang, T. Zhou, L. Wang, R.-J. Xie, A.C.S. Appl, Mater. Interfaces **14**, 16404 (2022)
154. F. Qin, M. Lu, S. Sun, P. Lu, N. Feng, Y. Gao, X. Bai, Z. Wu, J. Hu, Y. Zhang, IEEE Electron Device Lett. **44**, 1056 (2023)
155. T. Lee, G.W. Baek, G. Park, D. Shin, W.K. Bae, J. Kwak, IEEE J. Sel. Top. Quantum Electron. **30**, 2000107 (2023)
156. T. Park, D.C. Kim, J. Flex. Print. Electron. **2**, 211 (2023)
157. Z. Wu, P. Liu, W. Zhang, K. Wang, X.W. Sun, ACS Energy Lett. **5**, 1095 (2020)

applications.

on functional nanomaterials.

Tae-Woo Park received his B.S. (2023) from the Department of Electronic engineering at Gachon University. Under the supervision of Prof. Dong Chan Kim, he is working on the fabrication of stretchable electronic/optoelectronic devices.

Dae-Hyeong Kim received his B.S. (2000) and M.S. (2002) degrees from the School of Chemical Engineering at Seoul National University. He obtained his Ph.D. (2009) from the Department of Materials Science and Engineering at the University of Illinois at Urbana-Champaign. Since he joined the faculty of the School of Chemical and Biological Engineering at Seoul National University in 2011, he has focused on stretchable electronics for bio-medical, optical, and energy

Dong Chan Kim received his B.S. (2014) from the Department of Chemical and Biomolecular engineering at Korea Advanced Institute of Science and Technology (KAIST). He obtained his Ph.D. (2021) from the School of Chemical and Biological Engineering at Seoul National University. Since he joined the faculty of the Department of Chemical and Biological Engineering at Gachon University in 2023, he has focused on the fabrication of flexible and stretchable optoelectronic devices based